

Gravitational lensing by CDM halos: singular versus nonsingular profiles

Hugo Martel^{*} and Paul R. Shapiro[†]

Department of Astronomy, University of Texas, Austin, TX 78712

Submitted May 5 2003

ABSTRACT

The gravitational lensing properties of cosmological halos depend upon the mass distribution within each halo. The description of halos as nonsingular, truncated isothermal spheres, a particular solution of the isothermal Lane-Emden equation (suitably modified for $\Lambda \neq 0$), has proved to be a useful approximation for the halos which form from realistic initial conditions in a CDM universe. The nonsingular TIS model reproduces many of the quantitative features of the N-body results for CDM halos, except in the very center, where CDM N-body halos show density profiles which vary as $\rho \sim r^{-\alpha}$, $\alpha \gtrsim 1$, instead of a small flat core. Possible discrepancies between these cuspy halo predictions of the CDM N-body simulations and observations of the inner mass profiles of dwarf and LSB disk galaxies based upon their rotation curves and of clusters based upon strong lensing measurements have led to a search for other diagnostics. A description of the lensing by TIS halos would be useful in this regard, as a self-consistent model for CDM halos in a proper cosmological context, nonsingular but otherwise consistent with the CDM N-body results.

We derive here the basic lensing properties of individual TIS halos. For comparison, we also consider three singular profiles: the Navarro-Frenk-White density profile, the singular isothermal sphere, and the Schwarzschild lens. For all profiles, we compute the critical curves and caustics, the image separation, the magnification and brightness ratio, the shear, the time delay, and the average shear inside the tidal radius. This provides tools for studying the statistical properties of lensing by TIS and other lenses in the context of a theory of cosmological structure formation.

Key words: cosmology: theory – dark matter – galaxies: clusters: general – galaxies: formation – galaxies: halos – gravitational lensing

1 INTRODUCTION

The gravitational lensing of distant sources has in recent years become one of the most powerful tools in observational cosmology (see, for example, Soucail 2001 and references therein; Bartelmann & Schneider 2001 and references therein). Since the effects of gravitational lensing depend upon the redshift of the source, the cosmological background, and the distribution of matter in the universe, they can be used to constrain the cosmological parameters and the primordial power spectrum of density fluctuations from which structure originates. In addition, many of the effects produced by gravitational lenses, such as image multiplicity, separations, and time delay, depend strongly upon the matter distribution inside the lenses. Hence, measurements of these effects can provide a unique tool for probing the

matter distribution inside collapsed objects like galaxies and clusters, providing the only direct measurement of their dark matter content, and constraining the theory of their formation and evolution.

Until recently, the internal structure of halos adopted in lensing studies was generally some gravitational equilibrium distribution, either singular or nonsingular (e.g., King model, singular isothermal sphere, pseudo-isothermal sphere), not necessarily motivated directly by the theory of cosmological halo formation (see, e.g., Young et al. 1980; Turner, Ostriker, & Gott 1984; Hinshaw & Krauss 1987; Narayan & White 1988; Blandford et al. 1991; Jaroszyński 1991; Jaroszynski 1992; Kochanek 1995; Premadi, Martel, & Matzner 1998; Premadi et al. 2001a,b; Rusin & Ma 2001). As the theory of halo formation in the CDM model has advanced in recent years, however, the halo mass profiles adopted for lensing models have been refined to reflect this theory. Numerical simulations of large-scale structure formation in Cold Dark Matter

^{*} E-mail: hugo@simplicio.as.utexas.edu

[†] E-mail: shapiro@astro.as.utexas.edu

(CDM) universes predict that galaxies and clusters have a singular density profile which approaches a power law $\rho \propto r^{-n}$ at the center, with the exponent n ranging from 1 to 1.5 (Cole & Lacey 1996; Navarro, Frenk, & White 1996, 1997; Tormen, Bouchet, & White 1997; Fukushige & Makino 1997, 2001a,b; Moore et al. 1998, 1999; Huss, Jain, & Steinmetz 1999; Ghigna et al. 2000; Jing & Suto 2000; Klypin et al. 2000; Power et al. 2002). These results are in apparent conflict with observations of rotation curves of dark-matter-dominated dwarf galaxies and low surface brightness galaxies, which favor a flat-density core (cf. Primack et al. 1999; Burkert & Silk 1999; Moore et al. 1999; Moore 2001). On the scale of clusters of galaxies, observations of strong gravitational lensing of background galaxies by foreground clusters also favor the presence of a finite-density core in the centers of clusters (see, e.g., Tyson, Kochanski & Dell’Antonio 1998).

Several possible explanations have been suggested in order to explain this discrepancy. The rotation curve data might lack sufficient spatial resolution near the center to distinguish unambiguously between a density profile with a flat-density core and one with a singular profile (e.g. van den Bosch & Swaters 2001). Attempts have also been made to improve the numerical resolving power of the simulations to obtain a more accurate determination of the slope of the predicted density profiles at small radii (e.g. Moore et al. 1999; Power et al. 2002). However, if the flat-core interpretation of the observations and the singular cusps predicted by the numerical simulations are both correct, then the simulation algorithms may be ignoring some physical process which would, if included, serve to flatten the halo density profiles at small radii relative to the results for purely gravitational, N-body dynamics of cold, collisionless dark matter, while retaining the more successful aspects of the CDM model. For example, gasdynamical processes which involve dissipation and radiative cooling, and perhaps energy-release feedback associated with stars and quasars (see, e.g. Gelato & Sommer-Larsen 1999; El-Zant, Shlosman, & Hoffman 2001) or modifications of the microscopic properties of the dark matter, such as self-interacting dark matter (Spergel & Steinhardt 2000; Yoshida et al. 2000; Hannestad, & Scherrer 2000; Davé et al. 2001), warm dark matter (Colín, Avila-Reese, & Valenzuela 2000; Sommer-Larsen & Dolgov 2001), fluid dark matter (Peebles 2000), fuzzy dark matter (Hu, Barkana, & Gruzinov 2000), decaying dark matter (Cen 2001), annihilating dark matter (Kaplinghat, Knox, & Turner 2000), or repulsive dark matter (Goodman 2000), all have the potential to lower the central density of halos and possibly reconcile simulations with observations.

Lensing by the two kinds of halo mass profiles, singular versus flat-core, will be different. This has led to attempts to predict the differences expected if the halos have the singular cusp of the Navarro-Frenk-White (NFW) or Moore profiles or else a profile with a flat core (e.g. Kochanek 1995; Keeton & Madau 2001; Rusin & Ma 2001; Wyithe, Turner, & Spergel 2001; Takahashi & Chiba 2001; Li & Ostriker 2002). Singular profiles like that of NFW are physically motivated by the N-body simulations, and the latter have been used to place these halo profiles empirically in a proper cosmological context which permits statistical

predictions for the CDM model. The nonsingular profiles which have been adopted to contrast with these singular ones, however, are generally no more than parameterized, mathematical fitting formulae, with no particular physical model to motivate them or put them in a proper cosmological context.

We have developed an analytical model for the post-collapse equilibrium structure of virialized objects that condense out of a cosmological background universe, either matter-dominated or flat with a cosmological constant (Shapiro, Iliiev, & Raga 1999, hereafter Paper I; Iliiev & Shapiro 2001a, hereafter Paper II). This *Truncated Isothermal Sphere*, or TIS, model assumes that cosmological halos form from the collapse and virialization of “top-hat” density perturbations and are spherical, isotropic, and isothermal. This leads to a unique, nonsingular TIS, a particular solution of the Lane-Emden equation (suitably modified when $\Lambda \neq 0$). The size r_t and velocity dispersion σ_V are unique functions of the mass M and formation redshift z_{coll} of the object for a given background universe. The TIS density profile flattens to a constant central value, ρ_0 , which is roughly proportional to the critical density of the universe at the epoch of collapse, with a small core radius $r_0 \approx r_t/30$ (where $\sigma_V^2 = 4\pi G\rho_0 r_0^2$ and $r_0 \equiv r_{\text{King}}/3$, for the “King radius” r_{King} , defined by Binney & Tremaine 1987, p. 228).

Even though the TIS model does not produce the central cusp in the density profile of halos predicted by numerical CDM simulations at very small radii, it does reproduce many of the average properties of these halos quite well, suggesting that it is a useful approximation for the halos which result from more realistic initial conditions (Papers I, II; Iliiev & Shapiro 2001b and references therein). In particular, the TIS mass profile agrees well with the fit by NFW to N-body simulations (i.e. fractional deviation of $\sim 20\%$ or less) at all radii outside of a few TIS core radii (i.e. outside a King radius or so). It also predicts the internal structure of X-ray clusters found by N-body and gasdynamical simulations of cluster formation in the CDM model. For example, the TIS model reproduces to great accuracy the mass-temperature and radius-temperature virial relations and integrated mass profiles derived empirically from the simulations of cluster formation (Evrard, Metzler, & Navarro 1996). The TIS model also successfully reproduces to high precision the mass-velocity dispersion relation for clusters in CDM simulations of the Hubble volume by the Virgo Consortium (Evrard et al. 2002), including its dependence on redshift for different background cosmologies. The TIS model also correctly predicts the average value of the virial ratio in N-body simulations of halo formation in CDM.

The TIS profile matches the observed mass profiles of dark-matter-dominated dwarf galaxies. The observed rotation curves of dwarf galaxies are generally well fit by a density profile with a finite density core suggested by Burkert (1995), given by

$$\rho(r) = \frac{\rho_{0,B}}{(r/r_c + 1)(r^2/r_c^2 + 1)}. \quad (1)$$

The TIS model gives a nearly perfect fit to this profile, with best fit parameters $\rho_{0,B}/\rho_{0,\text{TIS}} = 1.216$, $r_c/r_{0,\text{TIS}} = 3.134$, correctly predicting the maximum rotation velocity v_{max} and the radius r_{max} at which it occurs. The TIS model can also explain the mass profile with a flat density core

measured by Tyson, Kochanski & Dell’Antonio (1998) for cluster CL 0024+1654 at $z = 0.39$, using the strong gravitational lensing of background galaxies by the cluster to infer the cluster mass distribution (Shapiro & Iliev 2000). The TIS model not only provides a good fit to the projected surface mass density distribution of this cluster within the arcs, but also predicts the overall mass, and a cluster velocity dispersion in close agreement with the value $\sigma_V = 1150$ km/s measured by Dressler et al. (1999).

Therefore, the TIS model can be applied to clusters of galaxies or dark-matter-dominated dwarf galaxies, for which baryonic processes have not significantly modified the mass profile. At the intermediate scale of large galaxies, where the central density profiles may be baryon-dominated, following radiative cooling by the baryon gas, the central profiles may differ from that of the halo of dark matter and baryons which would otherwise form in the absence of radiative losses by the baryonic gas. The TIS model ignores such processes, just as the empirical density profiles (NFW, Moore, ...) based on gravity-only N-body simulations do. Hence, these profiles might not be directly applicable to galaxy-scale objects for which the mass profiles have been significantly affected by such baryonic processes.

Several authors have studied the effect of lensing by halos with a flat-density core (Jaroszyński 1991; Jaroszyński 1992; Kochanek 1995; Premadi, Martel, & Matzner 1998; Premadi et al. 2001a,b) or by NFW or Moore profiles that have been generalized, so that the inner slope of the density profile is arbitrary (Keeton & Madau 2001; Rusin & Ma 2001; Wyithe, Turner, & Spergel 2001; Li & Ostriker 2002). These particular density profiles are essentially mathematical conveniences without physical motivation. There is no underlying theoretical model in these cases that was used to predict the value of the core radius or the departure of the inner slope of the density profile from the value found by N-body simulations of CDM. By contrast, the TIS model is based on a set of physical assumptions concerning the origin, evolution, and equilibrium structure of halos in CDM universes. Observations of gravitational lenses have the potential to distinguish between the TIS profile and singular ones like the NFW profile, as several observable properties of gravitational lenses will be strongly affected by the presence, or absence of a central cusp in the density profile. One example of an important observable that can distinguish between various density profiles is the parity of the number of images. Lenses with nonsingular density profiles, such as the TIS, obey the *odd number theorem*. The number of images of a given source is always odd, unless the source is extended and saddles a caustic (see Schneider, Ehlers, & Falco 1992, hereafter SEF, p. 172). Lenses with singular profiles, like the singular isothermal sphere, the NFW profile, or the Moore profile, need not obey this theorem, even for point sources. Most observed multiple-image gravitational lenses have either 2 or 4 images, and this may argue against profiles with a central core (Rusin & Ma 2001). There are, however, other possible explanations for the absence of a third or fifth image. That image tends to be very close to the optical axis, and might be hidden behind the lens itself. Also, it is usually highly demagnified, and might be too faint to be seen.

We can use the TIS solution to model observed gravitational lenses individually. Alternatively, we can use the observations collectively to constrain the distribution of halo

properties as characterized by the TIS solution. These properties, core radius, velocity dispersion, central density, and so on, depend upon the mass of the lensing halos and the redshift at which they form. Observational constraints on the statistical distribution of these properties will, in turn, impose constraints on the cosmological parameters and the primordial power spectrum of density fluctuations.

In this paper, we derive all the lensing properties of the TIS. We also compare the TIS with three other density profiles: The Navarro-Frenk-White (NFW) density profile, the Singular Isothermal Sphere (SIS), and the Schwarzschild Lens¹. To compare the lensing properties of these various lens models, we focus on one particular cosmological model, the currently favored COBE-normalized Λ CDM model with $\Omega_0 = 0.3$, $\lambda_0 = 0.7$, and $H_0 = 70$ km s⁻¹Mpc⁻¹ (this model is also cluster-normalized).

The remainder of this paper is organized as follows. In §2, we describe the TIS density profile and the various comparison profiles. In §3, we derive the lens equation. In §4, we compute the critical curves and caustics. In §5, we study the properties of multiple images: separation, magnification, brightness ratios, and time delay. In §6, we study the properties of weak lensing, focusing on the average shear. In §7, we discuss the likelihood of actually observing cases of strong lensing produced by TIS halos. Summary and conclusion are presented in §8.

2 THE DENSITY PROFILES

In order to compare the predictions for halo lensing for different halo density profiles, we must relate the parameters which define one profile to those which define another. For this purpose, we shall assume that all halo profiles contain the same total mass within a sphere of the same radius. The TIS halo is uniquely specified by the central density ρ_0 and core radius r_0 . The TIS halo has a well-defined outer radius r_t at which the mass distribution is truncated, enclosing a total mass M_t . There is a unique dimensionless density profile for the TIS if radius and density are expressed in units of r_0 and ρ_0 , respectively. Since the central density ρ_0 is proportional to $\rho_c(z_{\text{coll}})$, the critical density at the epoch of its formation, z_{coll} , it is also possible to specify the profile by the two parameters, total mass and collapse redshift, (M_t, z_{coll}) , which is equivalent to specifying the pair (r_0, ρ_0) . It is customary to define the total mass of other profiles used to model CDM halos as M_{200} , the mass inside a sphere of radius r_{200} with a mean density which is 200 times $\rho_c(z)$ at some redshift z . For the sake of direct comparison with the TIS profile, we will fix M_{200} and r_{200} for halos of different profiles, which amounts to fixing M_t and z_{coll} for the TIS halo, since $M_t = 1.167M_{200} = 772.6\rho_0 r_0^3$, $\rho_0 = 1.8 \times 10^4 \rho_c(z_{\text{coll}})$, and $r_{200} = 24.2r_0$ if $z = z_{\text{coll}}$.

For the NFW profile, there is a third parameter, the concentration parameter c , which must be specified in addition to the parameters M_{200} and r_{200} (or, equivalently, M_{200} and z). The value of c is not completely independent of the other parameters since there is a statistical expectation that

¹ A point mass

c is correlated with M_{200} and z . However, for any individual halo, c is not known a priori.

In what follows, we will consider two possibilities for comparing our TIS lens with other halo lens models. In the first case, the assumptions will be made that the lens redshift $z_L = z_{\text{coll}}$ for the TIS halo, and the concentration parameter c for the NFW halo of the same mass M_{200} and r_{200} at that redshift will be the typical value expected from the statistical correlation of c with halo mass and the redshift of observation of the halo, $z_{\text{obs}} = z_L$. In that case, the halos are fully specified by the values of M_{200} and z_L . In the second case, we can relax the assumption that $z_L = z_{\text{coll}}$. This makes the TIS halo a two-parameter model specified by $(M_{200}, z_{\text{coll}})$, and it is assumed that the halo which formed at some $z_{\text{coll}} \geq z_L$ did not evolve between z_{coll} and z_L . For the comparison NFW halo, we take the same M_{200} and r_{200} as the TIS halo, but allow the concentration parameter c to take any value, not necessarily the typical one for a halo of that mass M_{200} at redshift z_L . In what follows, we focus primarily on the first of these cases. This will illustrate the relative expectation of the TIS and other profile lenses in a sense which is conservative in regard to the possible strength of the strong lensing effects predicted by the TIS halos relative to the others. In our discussion, §7, we will then comment further on the effect of relaxing the assumption that $z_L = z_{\text{coll}}$, as discussed above.

2.1 The Radial Density Profiles

The density profile of the TIS is obtained numerically by solving a differential equation. However, it is well-fitted by the following approximation:

$$\rho(r) = \rho_0 \left(\frac{A}{a^2 + r^2/r_0^2} - \frac{B}{b^2 + r^2/r_0^2} \right) \quad (2)$$

(Paper I, II) where ρ_0 is a characteristic density, r_0 is a characteristic radius, and $A = 21.38$, $B = 19.81$, $a = 3.01$, $b = 3.82$. We will compute the lensing properties of halos with this density profile, and compare them with the properties derived for three comparison profiles. The first one is the Navarro, Frenk, and White (NFW) density profile,

$$\rho(r) = \frac{\rho_{\text{NFW}}}{(r/r_{\text{NFW}})(r/r_{\text{NFW}} + 1)^2}, \quad (3)$$

where ρ_{NFW} is a characteristic density and r_{NFW} is a characteristic radius. We will also consider the Singular Isothermal Sphere (SIS) density profile,

$$\rho(r) = \frac{\sigma_V^2}{2\pi G r^2}, \quad (4)$$

where σ_V is the velocity dispersion and G is the gravitational constant. This model might not represent actual halos very well, but it is a well-studied profile that has important theoretical value. Finally, for completeness, we will also consider the Schwarzschild lens,

$$\rho(r) = M_{\text{Sch}} \delta^3(r) \quad (5)$$

where M_{Sch} is the lens mass and δ^3 is the three-dimensional delta function.

To compare the lensing properties of these various density profiles, we use essentially the same approach as

Wright & Brainerd (2000). The virial radius r_{200} of a halo located at redshift z is defined, as usual, as being the radius inside which the mean density is equal to 200 times the critical density $\rho_c(z) \equiv 3H^2(z)/8\pi G$ at that redshift [where $H(z)$ is the Hubble parameter]. The mass M_{200} inside that radius is given by

$$M_{200} = \frac{800\pi\rho_c(z)r_{200}^3}{3}. \quad (6)$$

When comparing the lensing properties of different density profiles, we will consider halos that are located at the same redshift and have the same value of r_{200} . By definition, these halos will also have the same value of M_{200} . By stretching the terminology, we will refer to M_{200} as “the mass of the halo.” This point needs to be discussed. For the Schwarzschild lens, M_{200} is indeed the mass of the halo. The SIS density profile drops as r^{-2} at large r , and the mass therefore diverges unless we introduce a cutoff. The halo mass will then be equal to M_{200} only if the cutoff is chosen to be r_{200} . The NFW density profile drops as r^{-3} , hence the total mass diverges logarithmically, and this profile also needs a cutoff. The TIS density profile drops asymptotically as r^{-2} , but the TIS model includes a cutoff. This cutoff is located a radius $r_t \approx 1.2r_{200}$, and the mass inside the cutoff is $M_t = 1.168M_{200}$. In any case, a rigorous definition of the halo mass would require an unambiguous determination of the boundary between the halo and the background matter (such determination exists only for the TIS model), as well as dealing with the fact that the assumption of spherical symmetry that enters in these models most likely breaks down for real halos at large enough radii. Treating M_{200} as being the actual mass of the halo is the best compromise.

For a given halo mass M_{200} , redshift z , and cosmological background model, all density profiles are fully determined. The parameters of the various profiles (ρ_0 , r_0 , ρ_{NFW} , r_{NFW} , σ_V , and M_{Sch}) are computed as follows. First, we compute r_{200} using equation (6). The characteristic radius of the TIS is then given by

$$r_0 = r_{200}/\zeta_{200} = r_{200}/24.2 \quad (7)$$

(Paper I). The value $\zeta_{200} = 24.2$ is actually valid only for the Einstein-de Sitter model, but the dependence upon the cosmological model is rather weak (Paper II), and for simplicity we shall use the same value for all models. We now integrate equation (2) between $r = 0$ and $r = r_{200}$, and get

$$M_{200} = \frac{4\pi\rho_0 r_{200}^3 K_{200}}{\zeta_{200}^2}, \quad (8)$$

where

$$K_{200} \equiv A - B - \frac{aA}{\zeta_{200}} \arctan \frac{\zeta_{200}}{a} + \frac{bB}{\zeta_{200}} \arctan \frac{\zeta_{200}}{b} = 2.144 \quad (9)$$

(see also Chiba & Takahashi 2002, eq. [10]). By combining equations (6) and (8), we can eliminate M_{200} and r_{200} , and solve for ρ_0 . We get

$$\rho_0 = \frac{200\rho_c(z)\zeta_{200}^2}{3K_{200}} = 1.8 \times 10^4 \rho_c(z). \quad (10)$$

The characteristic radius of the NFW profile is given by

$$r_{\text{NFW}} = r_{200}/c, \quad (11)$$

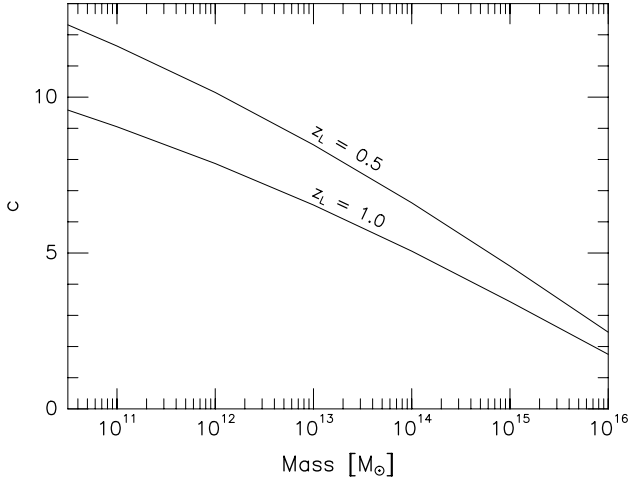


Figure 1. Concentration parameter c versus halo mass, for NFW halos located at redshifts $z_L = 0.5$ and 1.0 , as labeled.

where c is the concentration parameter. Unlike the case for the TIS, where r_{200}/r_0 is (nearly) constant, the concentration parameter of the NFW profile is strongly dependent upon the halo mass, redshift, and cosmological model. To determine c for a given halo, we use the formalism of Eke, Navarro, & Steinmetz (2001). According to this formalism, the concentration parameter in the Λ CDM model considered here varies with halo mass for two illustrative values of halo lens redshift $z_L = 0.5$ and 1.0 as shown in Figure 1. Once the value of c is known, we can compute the parameters of the profile. The characteristic density ρ_{NFW} is given by

$$\rho_{\text{NFW}} = \frac{200c^3 \rho_c(z)}{3[\ln(1+c) - c/(1+c)]}, \quad (12)$$

and the characteristic radius is given by equation (11) above. For the SIS, we integrate equation (4) between $r = 0$ and $r = r_{200}$, and get

$$M_{200} = \frac{2\sigma_V^2 r_{200}}{G}. \quad (13)$$

Combining equations (6) and (13), we get

$$\sigma_V = \sqrt{\frac{400\pi G \rho_c(z) r_{200}^2}{3}}. \quad (14)$$

Finally, M_{Sch} is given by M_{200} . Figure 2 shows a comparison of the various profiles, for halos with the same values of r_{200} , and M_{200} .

2.2 The Projected Surface Density

The projected surface density is given by

$$\Sigma(\xi) = \int_{-\infty}^{\infty} \rho(r) dz, \quad (15)$$

where ξ is the projected distance from the center of the halo, and $z = (r^2 - \xi^2)^{1/2}$. In principle, this expression can be used only if our expressions for $\rho(r)$ (eqs. [2]–[5]) are valid all the way to $r = \infty$. As we pointed out in the previous section, most profiles must be truncated at some finite radius r_t . For instance, the TIS is truncated at a truncation

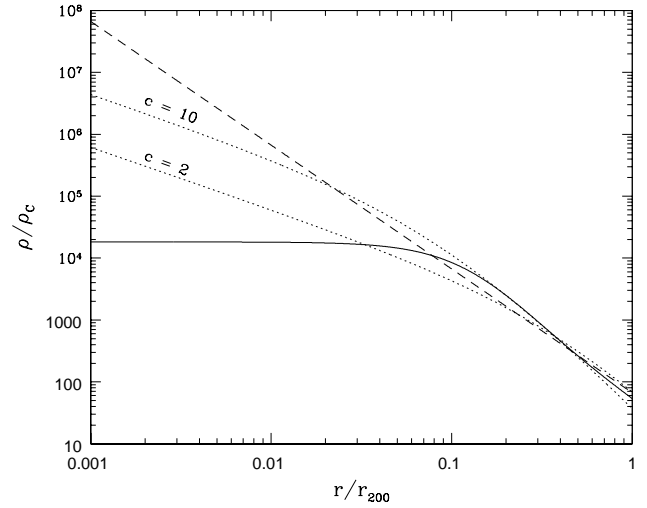


Figure 2. Radial density profiles, for 4 different halos with the same values of r_{200} and M_{200} . Solid curve: TIS; dotted curves: NFW profiles with concentration parameters $c = 2$ and 10 (as labeled); dashed curve: SIS.

radius $r_t \approx 30r_0$ (the actual value is 29.4 for an Einstein-de Sitter universe [Paper I], slightly different for an open matter-dominated universe, or a flat universe with a cosmological constant [Paper II]). One could always set the limits in equation (15) to $\pm(r_t^2 - \xi^2)^{1/2}$. However, it turns out that the resulting change in Σ would be small, for all profiles considered. To simplify the algebra, we shall assume that equation (15) remains a good approximation out to $r = \infty$. We substitute equations (2)–(5) in equation (15). For the TIS, we get

$$\Sigma_{\text{TIS}}(\xi) = \pi \rho_0 r_0^2 \left[\frac{A}{\sqrt{a^2 r_0^2 + \xi^2}} - \frac{B}{\sqrt{b^2 r_0^2 + \xi^2}} \right] \quad (16)$$

[This result was also derived by Natarajan, & Lynden-Bell (1997), and Iliev (2000)]. For the NFW profile, we get

$$\Sigma_{\text{NFW}}(\xi) = 2r_{\text{NFW}} \rho_{\text{NFW}} \times \begin{cases} \frac{1}{x^2 - 1} \left[1 - \frac{2}{\sqrt{1-x^2}} \arg \tanh \sqrt{\frac{1-x}{1+x}} \right], & x < 1; \\ 1/3, & x = 1; \\ \frac{1}{x^2 - 1} \left[1 - \frac{2}{\sqrt{x^2 - 1}} \arctan \sqrt{\frac{x-1}{x+1}} \right], & x > 1; \end{cases} \quad (17)$$

where $x = \xi/r_{\text{NFW}}$ (Bartelmann 1996; Wright & Brainerd 2000). For the SIS, we get

$$\Sigma_{\text{SIS}}(\xi) = \frac{\sigma_V^2}{2G\xi}. \quad (18)$$

Finally, for the Schwarzschild Lens, we get

$$\Sigma_{\text{Sch}}(\xi) = M_{\text{Sch}} \delta^2(\xi). \quad (19)$$

2.3 The Interior Mass Profile

For spherically symmetric lenses, one important quantity is the interior mass $M(\xi)$ inside a cylinder of projected radius ξ centered around the center of the lens. This quantity is given by

$$M(\xi) = 2\pi \int_0^\xi \Sigma(\xi') \xi' d\xi'. \quad (20)$$

We have computed this expression for all density profiles considered, using equations (16)–(19). We also reexpressed the results in units of M_{200} with the help of the equations given in §2.1. For the TIS, we get

$$M_{\text{TIS}}(\xi) = \frac{\pi M_{200}}{2\zeta_{200} K_{200}} \left[A \sqrt{a^2 + \xi^2/r_0^2} - B \sqrt{b^2 + \xi^2/r_0^2} - Aa + Bb \right]. \quad (21)$$

For the NFW profile, we get

$$M_{\text{NFW}}(\xi) = 4\pi r_{\text{NFW}}^3 \rho_{\text{NFW}} g(\xi/r_{\text{NFW}}), \quad (22)$$

where

$$g(x) = \begin{cases} \frac{2}{\sqrt{1-x^2}} \arg \tanh \sqrt{\frac{1-x}{1+x}} + \ln \frac{x}{2}, & x < 1; \\ 1 + \ln \frac{1}{2}, & x = 1; \\ \frac{2}{\sqrt{x^2-1}} \arctan \sqrt{\frac{x-1}{x+1}} + \ln \frac{x}{2}, & x > 1; \end{cases} \quad (23)$$

(Wright & Brainerd 2000; Chiba & Takahashi 2002). For the SIS, we get

$$M_{\text{SIS}}(\xi) = \frac{\pi M_{200} \xi}{2r_{200}}. \quad (24)$$

Finally, for the Schwarzschild lens, we get

$$M_{\text{Sch}}(\xi) = M_{200}. \quad (25)$$

Figure 3 shows a comparison of $M(\xi)$ for various halos with the same values of r_{200} and M_{200} .

3 THE LENS EQUATION

Figure 4 illustrates the lensing geometry. The quantities η and ξ are the position of the source on the source plane and the image on the image plane, respectively, $\hat{\alpha}$ is the deflection angle, and D_L , D_S , and D_{LS} are the angular diameter distances between observer and lens, observer and source, and lens and source, respectively. The lens equation is

$$\eta = \frac{D_S}{D_L} \xi - D_{LS} \hat{\alpha} \quad (26)$$

[SEF, eq. (2.15b)]. Notice that since the lens is axially symmetric, we can write the quantities η , ξ , and $\hat{\alpha}$ as scalars instead of 2-component vectors. We introduce a characteristic length scale ξ_0 , and nondimensionalize the positions and deflection angle, as follows:

$$y = \frac{D_L \eta}{D_S \xi_0}, \quad (27)$$

$$x = \frac{\xi}{\xi_0}, \quad (28)$$

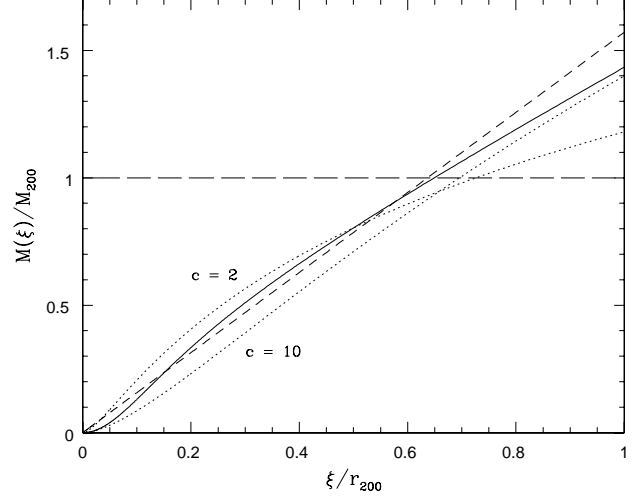


Figure 3. Interior mass profiles, for 5 different halos with the same values of r_{200} and M_{200} . Solid curve: TIS; dotted curves: NFW profiles with concentration parameters $c = 2$ and 10 (as labeled); short-dashed curve: SIS; long-dashed curve: Schwarzschild lens.

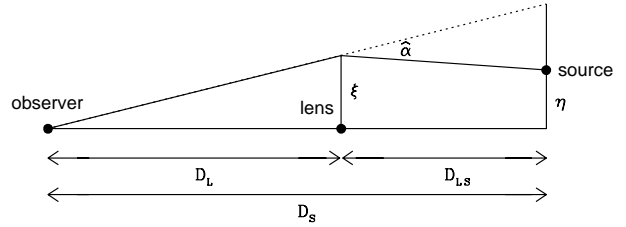


Figure 4. The lensing geometry: the dots indicate the location of the observer, lensing galaxy, and source. ξ and η are the positions of the image and the source, respectively, and $\hat{\alpha}$ is the deflection angle. The angular diameter distances D_L , D_{LS} , and D_S are also indicated.

$$\alpha = \frac{D_L D_{LS} \hat{\alpha}}{D_S \xi_0}. \quad (29)$$

The lens equation reduces to

$$y = x - \alpha(x). \quad (30)$$

For spherically symmetric lenses, the deflection angle is given by

$$\alpha(x) = \frac{2}{x} \int_0^x x' \frac{\Sigma(x')}{\Sigma_{\text{crit}}} dx' = \frac{2}{x} \int_0^x x' \kappa(x') dx' \quad (31)$$

[SEF, eq. (8.3)], where $\kappa \equiv \Sigma/\Sigma_{\text{crit}}$ is the convergence, and Σ_{crit} is the critical surface density, given by

$$\Sigma_{\text{crit}} = \frac{c^2 D_S}{4\pi G D_L D_{LS}}, \quad (32)$$

where c is the speed of light and D_L , D_S , and D_{LS} are the angular diameter distances between observer and lens, observer and source, and lens and source, respectively. From equations (20) and (31), we get

$$\alpha(x) = \frac{M(\xi_0 x)}{\pi \xi_0^2 \Sigma_{\text{crit}} x}. \quad (33)$$

Hence, the deflection angle is directly related to the interior mass. For the TIS, we substitute equation (21) into equation (33), and set the characteristic scale ξ_0 equal to r_0 . We get

$$\alpha_{\text{TIS}}(x) = \frac{2\pi\rho_0 r_0}{\Sigma_{\text{crit}} x} \left[A\sqrt{a^2 + x^2} - B\sqrt{b^2 + x^2} - Aa + Bb \right]. \quad (34)$$

This result was also obtained by Chiba & Takahashi (2001). We now introduce the dimensionless central surface density, or central convergence, κ_c , defined by

$$\kappa_c \equiv \frac{\Sigma(\xi=0)}{\Sigma_{\text{crit}}} = \frac{\pi\rho_0 r_0}{\Sigma_{\text{crit}}} \left(\frac{A}{a} - \frac{B}{b} \right), \quad (35)$$

and use this expression to eliminate Σ_{crit} in equation (34). It reduces to

$$\alpha_{\text{TIS}}(x) = \frac{2ab\kappa_c}{(Ab - Ba)x} \left[A\sqrt{a^2 + x^2} - B\sqrt{b^2 + x^2} - Aa + Bb \right]. \quad (36)$$

For the NFW profile, we substitute equation (22) into equation (33), and set $\xi_0 = r_{\text{NFW}}$. We get

$$\alpha_{\text{NFW}}(x) = \frac{4\kappa_s g(x)}{x} \quad (37)$$

where

$$\kappa_s \equiv \frac{\rho_{\text{NFW}} r_{\text{NFW}}}{\Sigma_{\text{crit}}}. \quad (38)$$

For the SIS profile, we substitute equation (24) into equation (33), and set

$$\xi_0 = \frac{4\pi\sigma_V^2 D_L D_{LS}}{c^2 D_S} = \frac{\sigma_V^2}{G\Sigma_{\text{crit}}}. \quad (39)$$

We get

$$\alpha_{\text{SIS}}(x) = \frac{x}{|x|} \quad (40)$$

(SEF, §8.1.4). Finally, for the Schwarzschild lens, we set $M(\xi_0 x) = M_{\text{Sch}}$ and

$$\xi_0 = \sqrt{\frac{4GM_{\text{Sch}} D_L D_{LS}}{c^2 D_S}} = \sqrt{\frac{M_{\text{Sch}}}{\pi\Sigma_{\text{crit}}}}. \quad (41)$$

We get

$$\alpha_{\text{Sch}}(x) = \frac{1}{x} \quad (42)$$

(SEF, §8.1.2).

4 CRITICAL CURVES AND CAUSTICS

4.1 Solutions

The determination of the critical curves is quite trivial for axially symmetric lenses. Equation (33) can be rewritten as

$$m(x) \equiv \alpha(x)x \quad (43)$$

[SEF, eq. (8.3)], where $m(x) = M(\xi_0 x)/\pi\xi_0^2\Sigma_{\text{crit}}$ is the dimensionless interior mass. Tangential and radial critical curves are defined respectively by

$$\frac{m(x_t)}{x_t^2} \equiv \frac{\alpha(x_t)}{x_t} = 1, \quad (44)$$

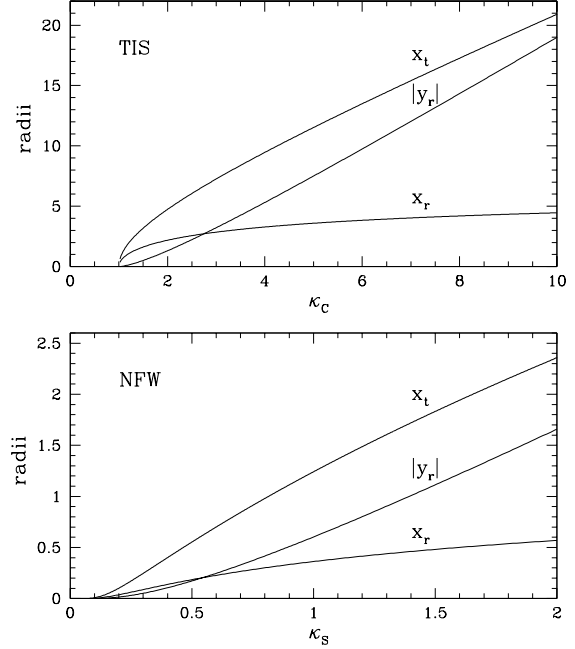


Figure 5. Top panel: Radii of the radial critical circle, x_r , tangential critical circle, x_t , and radial caustic, y_r , versus κ_c , for the TIS. Bottom panel: x_t , x_r , and y_r versus κ_s , for the NFW profile.

$$\left[\frac{d(m/x)}{dx} \right]_{x=x_r} \equiv \left[\frac{d\alpha}{dx} \right]_{x=x_r} = 1. \quad (45)$$

For the Schwarzschild lens and the SIS, the solutions are $x_t = 1$, and there are no real solutions for x_r . For the NFW and TIS models, we have solved equations (44) and (45) numerically for x_t and x_r . The solutions are plotted in Figure 5, as functions of κ_c and κ_s . Also plotted is the radial caustic radius y_r , obtained by substituting the value of x_r into equation (30). (The value of y_r we obtain is actually negative, because the source and image are on opposite sides of the lens. The actual radius of the caustic circle, then, is the absolute value of y_r .) Both x_t and $|y_r|$ increase rapidly with κ_c or κ_s , while the value of x_r levels off. Notice that there is no relation between κ_c and κ_s . The former is the central convergence of the TIS, while the latter is the convergence of the NFW profile at some finite radius and its value depends upon the concentration parameter c . Figure 6 shows the angular radii of the tangential and radial critical circles, $\theta_r = \xi_r/D_L$ and $\theta_t = \xi_t/D_L$, in arc seconds as functions of the mass of the lens, for lenses located at redshifts $z_L = 0.5$ and 1. We assume that the source is located at redshift $z_S = 3$. This is not a very constraining assumption, because the lensing properties vary weakly with the source redshift for $z_S \gg 1$. For instance, for lenses located at redshifts $z_L \leq 1$, the critical surface density Σ_{crit} varies by less than 20% when the source is moved from $z_S = 3$ to $z_S = 5$.

For spherically symmetric lenses, multiple images (and thus critical circles) are possible only if the central convergence $\kappa(0)$ exceeds unity (SEF, p. 236, theorem [e]). For the Schwarzschild lens, SIS, and NFW profile, the central convergence diverges, hence these profiles can always produce multiple images. But for the TIS, the central convergence

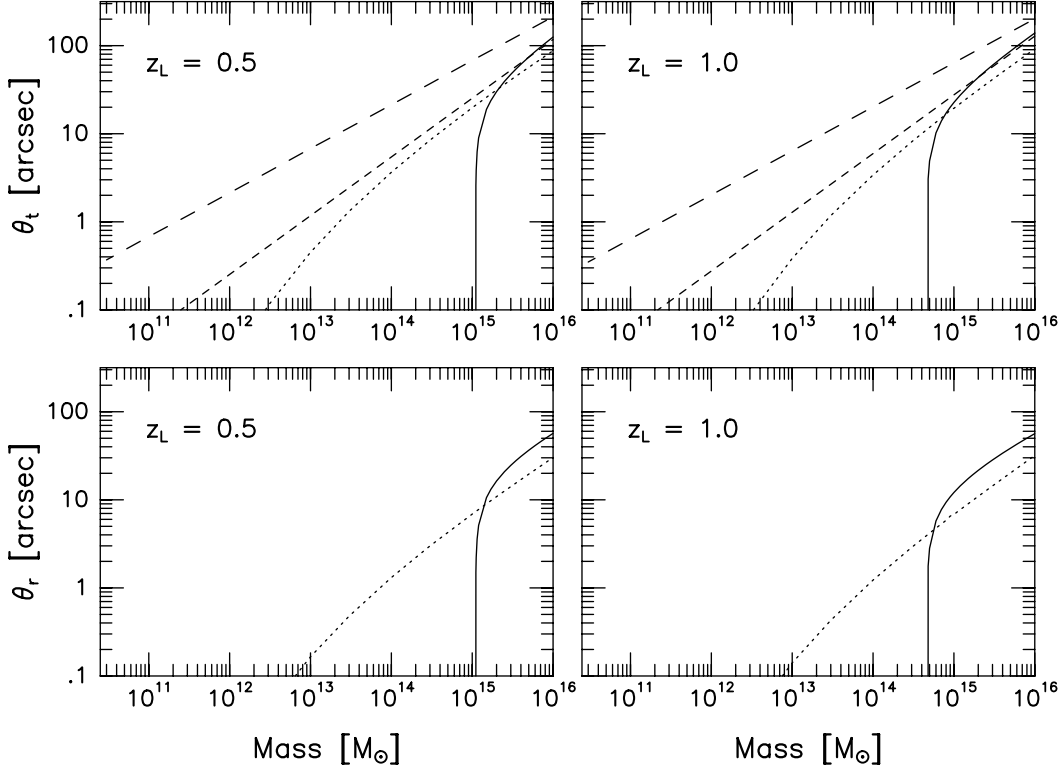


Figure 6. Angular radius of the tangential critical curve (top) and radial critical curve (bottom), versus lens mass, for the TIS (solid curves), the NFW profile (dotted curves), the SIS (short dashed curves) and the Schwarzschild lens (long dashed curves). Results are shown for lenses located at redshift $z_L = 0.5$ (left panels) and 1 (right panels).

$\kappa(0) \equiv \kappa_c$ is finite, and multiple images can be produced only if $\kappa_c > 1$. This explains the sharp low-mass cutoff seen in Figure 6 for the TIS (solid curves).

The value of θ_t for the Schwarzschild lens is called the Einstein radius θ_E . It is often used to estimate the characteristic scale of image features caused by strong lensing (e.g. ring radius, radial location of arc, image separations) and to estimate the size of the region within which the mass responsible for that strong lensing must be concentrated. Since lensing halos are not actually point masses, however, the angular radius θ_{ring} of the actual Einstein ring which results if the source is located along the line of sight through the lens center will usually differ from the Einstein radius θ_E , assuming that the lens mass distribution is actually capable of producing a ring. As we see in Figure 6, θ_E significantly exceeds θ_t for all profiles considered (TIS, NFW profile, and SIS) for all masses considered. Hence, a mass estimate based on assuming that the scale of image features is of order θ_E will underestimate the actual mass of the lens, unless the lens happens to be a Schwarzschild lens.

A source located behind the lens will produce multiple images if $y < y_r$. The angular cross section for multiple imaging is therefore

$$\sigma_{\text{m.i.}} = \pi \left(\frac{\eta_r}{D_S} \right)^2 = \pi \left(\frac{y_r \xi_0}{D_L} \right)^2. \quad (46)$$

In Figure 7, we plot the ratio of the cross sections for the NFW and TIS profiles, for sources located at $z_S = 3$. At low

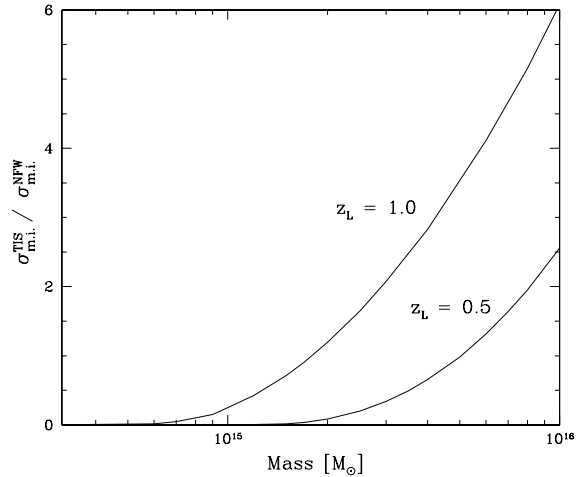


Figure 7. Ratio of the cross sections for multiple imaging by the TIS and the NFW profile, versus lens mass, for lenses located at redshift $z_L = 0.5$ and 1.

masses, $M < 5 \times 10^{15} M_\odot$ for $z_L = 0.5$, $M < 2 \times 10^{15} M_\odot$ for $z_L = 1.0$, the ratios are less than unity, indicating that a distribution of lenses described by the NFW profile would be more likely to produce cases with multiple images than if the same distribution is described by the TIS model. This trend

is reversed at higher masses, and a TIS of mass $M = 10^{16} M_\odot$ at $z_L = 1.0$ is 6 times more likely to produce multiple images than a NFW profile of the same mass.

4.2 Illustrative Example

Using a simple ray-tracing algorithm, we computed the image(s) of a circular source of diameter $\Delta y = 1$, created by a TIS with central convergence $\kappa_c = 4.015$. The results are shown in Figure 8 for 8 different locations of the source, ranging from $y = 8.0$ to $y = 0.0$. For each case, the left panel shows the source and the caustic circle ($y_r = 5.640$) on the source plane, and the right panel shows the image(s), the radial critical circle ($x_r = 3.334$), and the tangential critical circle ($x_t = 9.783$) on the image plane. For the cases $y = 8.0$ and 6.0 , only one image appears. At $y = 5.4$, the source overlaps the caustic, and a second, radially-oriented image appears on the radial critical circle. At $y = 4.8$, the source is entirely inside the caustic, and the second image splits in two images, located on opposite sides of the radial critical circle, forming with the original image a system of 3 aligned images. As the source moves toward $y = 0$, the central image moves toward $x = 0$ and becomes significantly fainter, while the other images move toward the tangential critical circle and become bright, elongated arcs. At $y = 0$, the two arcs have merged to form an Einstein ring located on top of the tangential critical circle, while the central image, very faint, is still visible in the center.

In the case of the TIS and the NFW profile, the radial caustics separate regions on the source plane according to the number of images a source in those regions produces, and when a source moves across such caustic, the number of images changes. A curve on the source plane that has this property is not always a caustic, although in the case of the NFW and TIS profiles, it is. A SIS will produce two images if $y < 1$, and one image if $y > 1$. However, the circle defined by $y = 1$ is not a caustic. When a source moves inside that circle, a second image appears at $x = 0$, but this value of x does not satisfy equation (45), and in particular the magnification does not diverge at $x = 0$, as in the case of a critical curve, but vanishes instead. Indeed, the total magnification varies smoothly and monotonically as a source moves across the $y = 1$ circle. For the Schwarzschild lens, there is no radial caustic, and this lens always produces two images, no matter where the source is. This happens because $\alpha(x)$ diverges as $x \rightarrow 0$ (eq. [42]), so no matter how large the angular separation between source and lens is, some rays will always be deflected toward the observer. However, for large separations, the second image is demagnified by an enormous factor.

5 PROPERTIES OF MULTIPLE IMAGES

5.1 Image Separation

The locations of the images are computed by solving the lens equation (30). For the Schwarzschild lens, the solutions are

$$x_{1,2} = \frac{y \pm \sqrt{y^2 + 4}}{2} \quad (47)$$

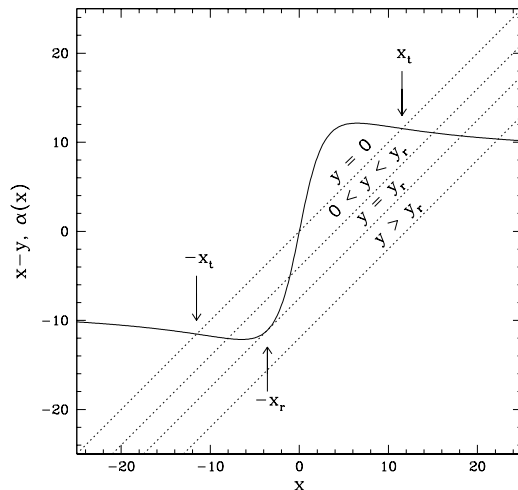


Figure 9. Plot of $\alpha(x)$ (solid curve) and $x - y$ (dotted lines) versus x , for a TIS with $\kappa_c = 5.005$ and 4 particular values of y : $y = 0$ (top line), $y = 4$, $y = y_r = 7.515$, and $y = 12$ (bottom line). Images are located at values of x corresponding to intersections between the lines and the curve. Particular solutions, corresponding to images located on critical curves, are indicated by arrows.

(SEF, eq. [8.28]). Hence, there are always two images, with separation

$$(\Delta x)_{\text{Sch}} = \sqrt{y^2 + 4}. \quad (48)$$

For the SIS, the solutions are

$$x_{1,2} = y \pm 1 \quad (49)$$

(SEF, eq. [8.34c]). Again, there are always two images, with separation

$$(\Delta x)_{\text{SIS}} = 2. \quad (50)$$

It is an interesting property of the SIS that the separation is independent of the source location. For the NFW profile and the TIS, the lens equation must be solved numerically. In Figure 9, we show the *multiple image diagram* for the particular case of a TIS with $\kappa_c = 5.005$. The solid curves show $\alpha(x)$, while the dotted lines show $x - y$ for particular values of y . Each intersection between a line and the curve corresponds to one image (see equation [30]). If $y > y_r$ (bottom line), the source is outside the caustic circle, and only one image appears. If $y = y_r$ the source is on the caustic circle and a second image appears on the radial critical circle, at $x = -x_r$. For $y < y_r$, the source is inside the caustic, and the second image splits into two images. Finally, for $y = 0$ (top curve), the central image is located at $x = 0$, and the two outer images are located on the tangential circle, at $x = \pm x_t$. Actually, these two images merge to form an Einstein ring. The slope of the curve $\alpha(x)$ versus x is equal to κ_c at $x = 0$. It is clear from Figure 9 that if we lower κ_c below 1, any $x - y$ versus x line will intersect the curve only once; multiple images cannot occur if $\kappa_c < 1$. The corresponding diagram for the NFW profile is qualitatively similar. However, in that case the slope of the curve $\alpha(x)$ versus x diverges at $x = 0$, hence there can always be 3 images, provided that the source is located inside the radial caustic

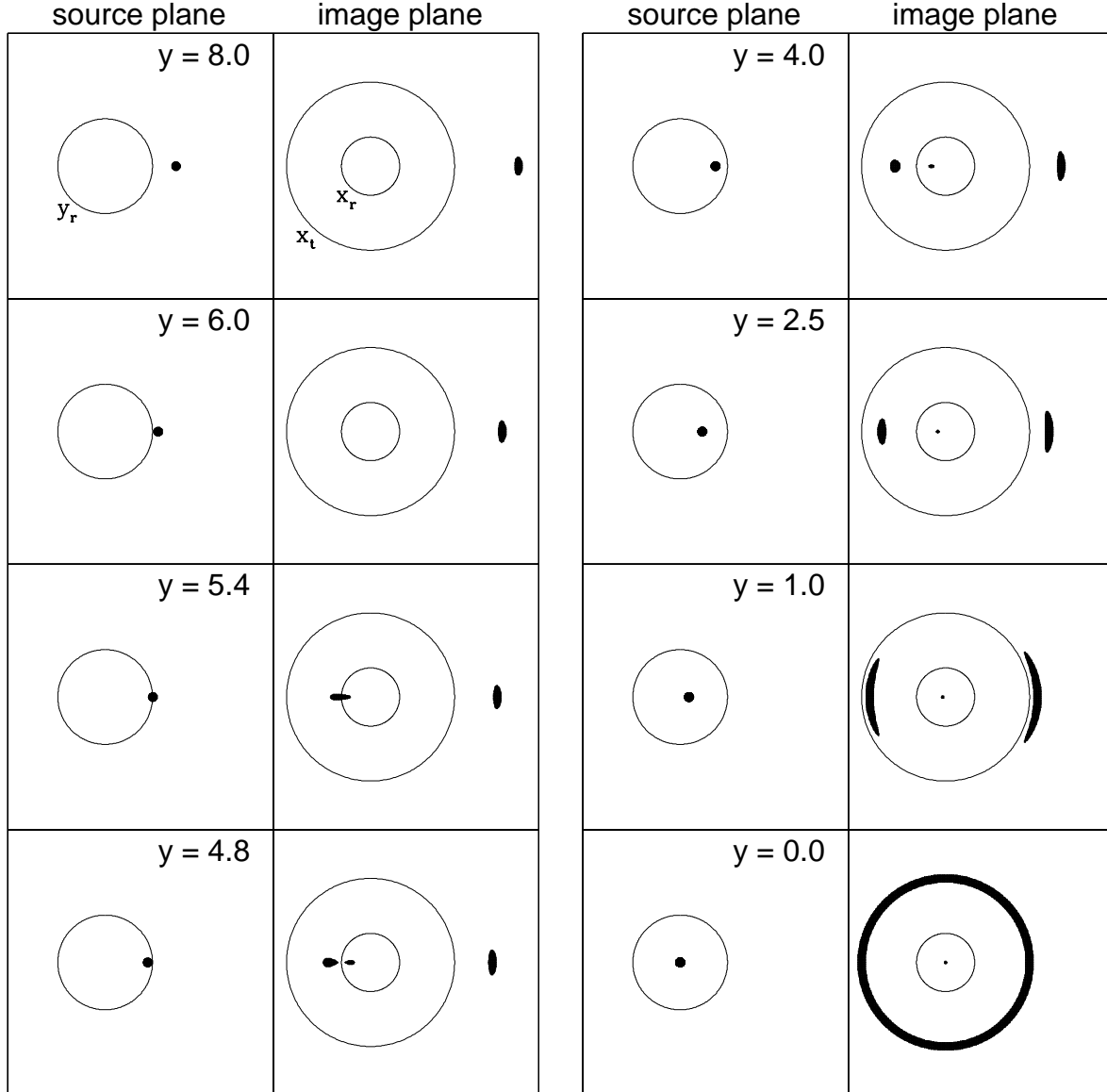


Figure 8. Images of a circular source. Each pair of panels shows the source plane in the left panel, with the caustic, and the image plane in the right panel, with the radial (inner) and tangential (outer) critical circles. The position y of the source on the source plane is indicated. We used $\kappa_c = 4.014$, and a source of diameter $\Delta y = 1$.

In Figure 10, we plot the separation between the two outer images as a function of the source location. The plot only extends to $y/y_r = 1$, since larger values of y only produce one image. The solid and dotted curves show the separations for the TIS and NFW profile, respectively, with various values of κ_c and κ_s . The separation is fairly insensitive to the source location, and stays within $\sim 15\%$ of the Einstein ring diameter $\Delta x = 2x_t$ for all values of κ_c and κ_s considered. For the SIS and Schwarzschild lens, y_r is undefined. The dashed line in Figure 10 shows the constant separation for the SIS. For the Schwarzschild lens the separation depends upon y , and therefore cannot be plotted in Figure 10 since y_r is undefined. However, in the limit of large y , it can be shown that the magnification of the faintest image drops as $1/y^4$ (see SEF, eq. [8.29a]). Hence, in practice, the second image will be visible only if y is small, in which

case equation (48) shows that the separation is close to $2x_t$, since $x_t = 1$ for that lens.

Therefore, for all profiles considered, the image separation is always of order the Einstein ring diameter, independently of the source location. This is particularly convenient for theoretical studies, when the actual source location can be ignored (see, e.g., Martel, Premadi, & Matzner 2002).

5.2 Magnification and Brightness Ratios

The magnification of an image located at position x on the lens plane is given by

$$\begin{aligned} \mu &= \left(1 - \frac{m}{x^2}\right)^{-1} \left[1 - \frac{d}{dx} \left(\frac{m}{x}\right)\right]^{-1} \\ &= \left(1 - \frac{\alpha}{x}\right)^{-1} \left(1 - \frac{d\alpha}{dx}\right)^{-1} \end{aligned} \quad (51)$$

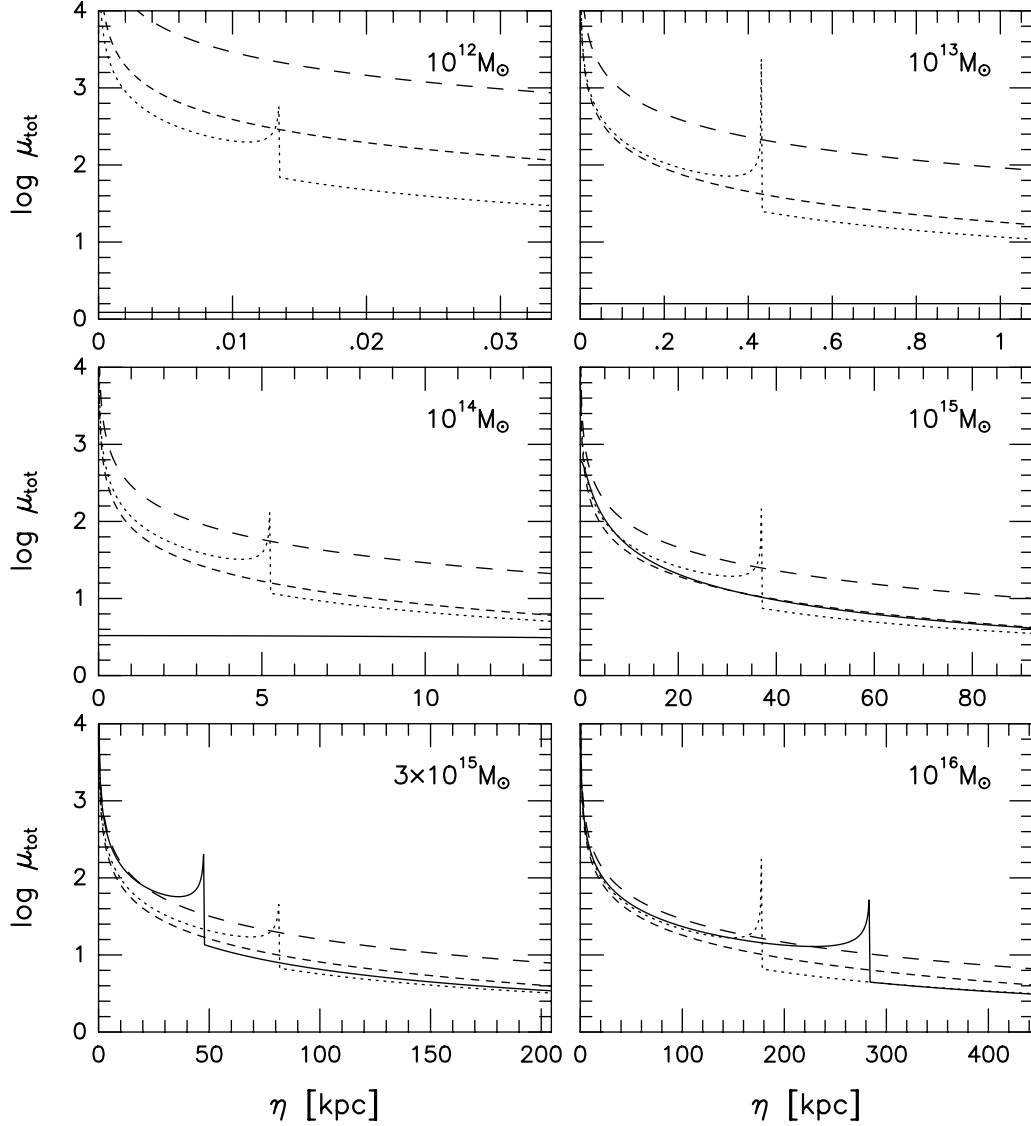


Figure 11. Total magnification μ_{tot} versus source location η for lenses of masses $10^{12} - 10^{16} M_{\odot}$ located at $z_L = 0.5$, for the TIS (solid curves), the NFW profile (dotted curves), the SIS (short dashed curves) and the Schwarzschild lens (long dashed curves).

(SEF, eq. [8.17]). We computed the magnification of the images produced by halos of masses 10^{12} , 10^{13} , 10^{14} , 10^{15} , 3×10^{15} , and $10^{16} M_{\odot}$ located at redshifts $z_L = 0.5$ and $z_L = 1$, for sources located at redshift $z_S = 3$. The results are plotted in Figures 11–15 as functions of the source position. Figures 11 and 12 show the total magnification. The dotted curves show the results for a NFW profile. As y (or η) decreases, the magnification slowly increases, until the source reaches the radial caustic $y = y_r$. At that moment, a second image, with infinite magnification ($1 - d(m/x)/dx = 0$ in eq. [51]) appears on the radial critical curve (for clarity, we truncated those infinite “spikes” in Figs. 11 and 12). As y keeps decreasing, that second image splits into two images, and the total magnification becomes finite again, until the source reaches $y = 0$, and an Einstein ring with infinite magnification ($1 - m/x^2 = 0$ in eq. [51]) appears on the tangential critical curve. Of course, these infinite magnifica-

tions are not physical, since they can only occur for point sources. The total magnification is always larger than unity, and always larger when 3 images are present.

The solid curves in Figures 11 and 12 show the results for the TIS. At low masses, there is no radial caustic (See Fig. 6), and only one image appears. Because of the presence of a flat density core, the magnification is nearly constant if the path of the rays goes near the center of the core. For instance, for the case $M_{200} = 10^{12} M_{\odot}$, $z_L = 0.5$ (top left panel of Fig. 11), $r_0 = 7.125$ kpc, hence, over the range of η being plotted, we are way inside the core. As the mass increases, the magnification increases, until a radial caustic forms. This happens at $M_{200} = 1.11 \times 10^{15} M_{\odot}$ for $z_L = 0.5$, and at $M_{200} = 4.7 \times 10^{15} M_{\odot}$ for $z_L = 1$, according to Figure 6. At this point, the TIS has the ability to form three images, and the results become qualitatively similar to the ones for the NFW profile.

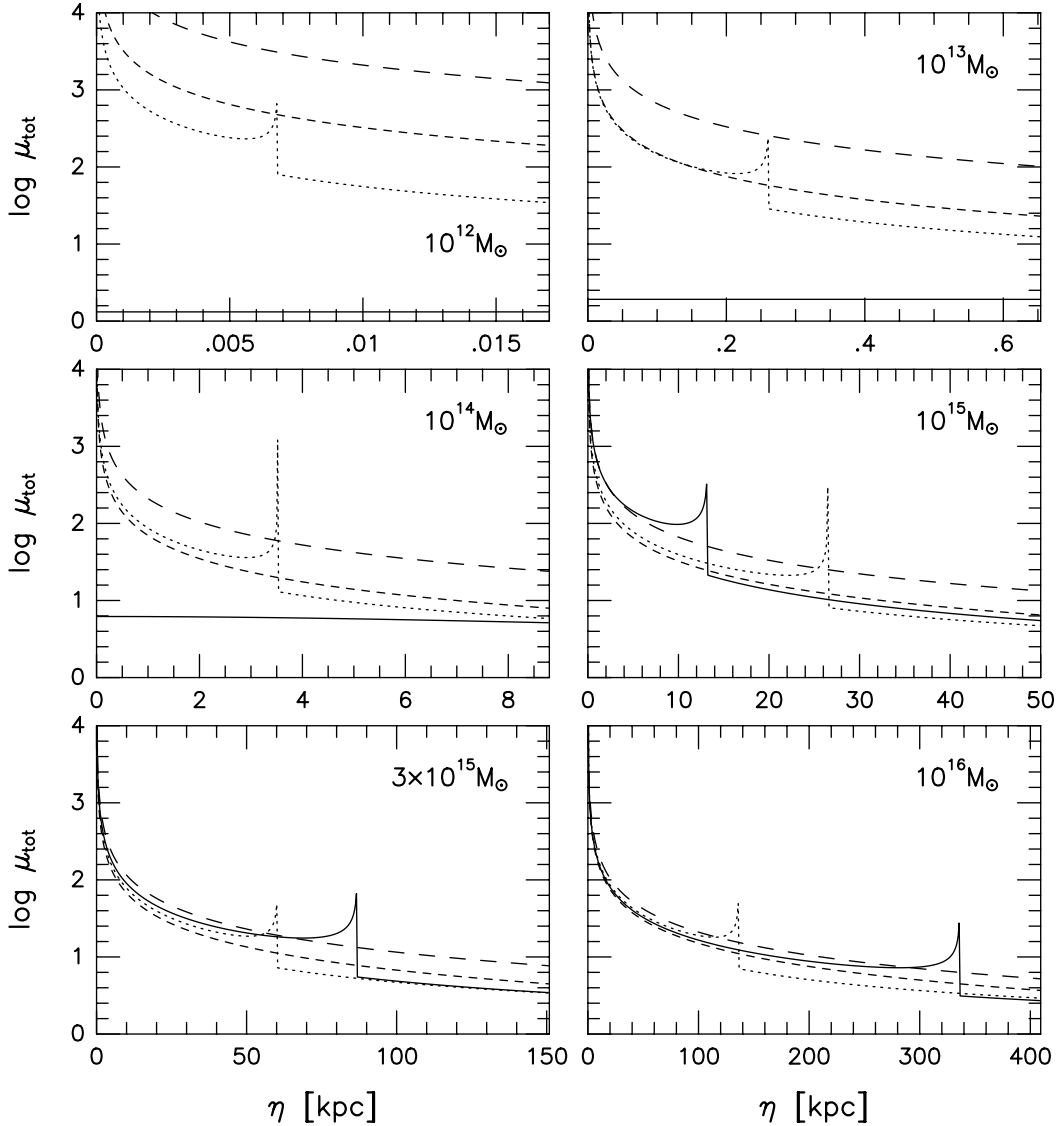


Figure 12. Total magnification μ_{tot} versus source location η for lenses of masses $10^{12} - 10^{16} M_{\odot}$ located at $z_L = 1.0$, for the TIS (solid curves), the NFW profile (dotted curves), the SIS (short dashed curves) and the Schwarzschild lens (long dashed curves).

The short-dashed and long-dashed curves in Figures 11 and 12 show the results for the SIS and the Schwarzschild lens, respectively. Because of the absence of radial caustic, the magnification always varies smoothly with source position, and the only divergence occurs at $\eta = 0$, where an Einstein ring forms.

For a given mass, the Schwarzschild lens always produces the strongest magnification, unless the source is very close to the radial caustic of a TIS or a NFW profile, where a “spike” of infinite magnification forms. At small masses ($M_{200} = 10^{12} M_{\odot}$), the SIS produces a stronger magnification than the NFW profile, for all source positions. However, at larger masses, we find a different behavior: If the NFW profile produces only one image (that is, we are on the right hand side of the dotted spike in Fig. 11 and 12), the SIS still produces a larger magnification than the NFW profile. But if the NFW profile produces 3 images, then the total

magnification exceeds the one produced by the SIS. As for the TIS, at low masses, where only one image forms, the magnification is much smaller than for the other profiles. But at large masses, where multiple images can form, the magnification becomes comparable to the one for the other profiles.

Figures 13, 14, and 15 show the brightness ratios $|\mu_1/\mu_3|$, and $|\mu_2/\mu_3|$, where μ_i is the magnification of image i , as a function of source position. By convention, image 1 is the one between the tangential and radial critical curves, image 2 is the one inside the radial critical curve, and image 3 is the one outside the tangential critical curve (see Fig. 8; from left to right, the three images are image 1, 2, and 3). The ratio $|\mu_1/\mu_3|$, plotted in Figures 13 and 14, always goes to unity in the limit $\eta \rightarrow 0$, as images 1 and 3 merge to form an Einstein ring. For $\eta > 0$, image 1 is usually fainter than image 3 ($|\mu_1/\mu_3| < 1$), unless it is located near the radial

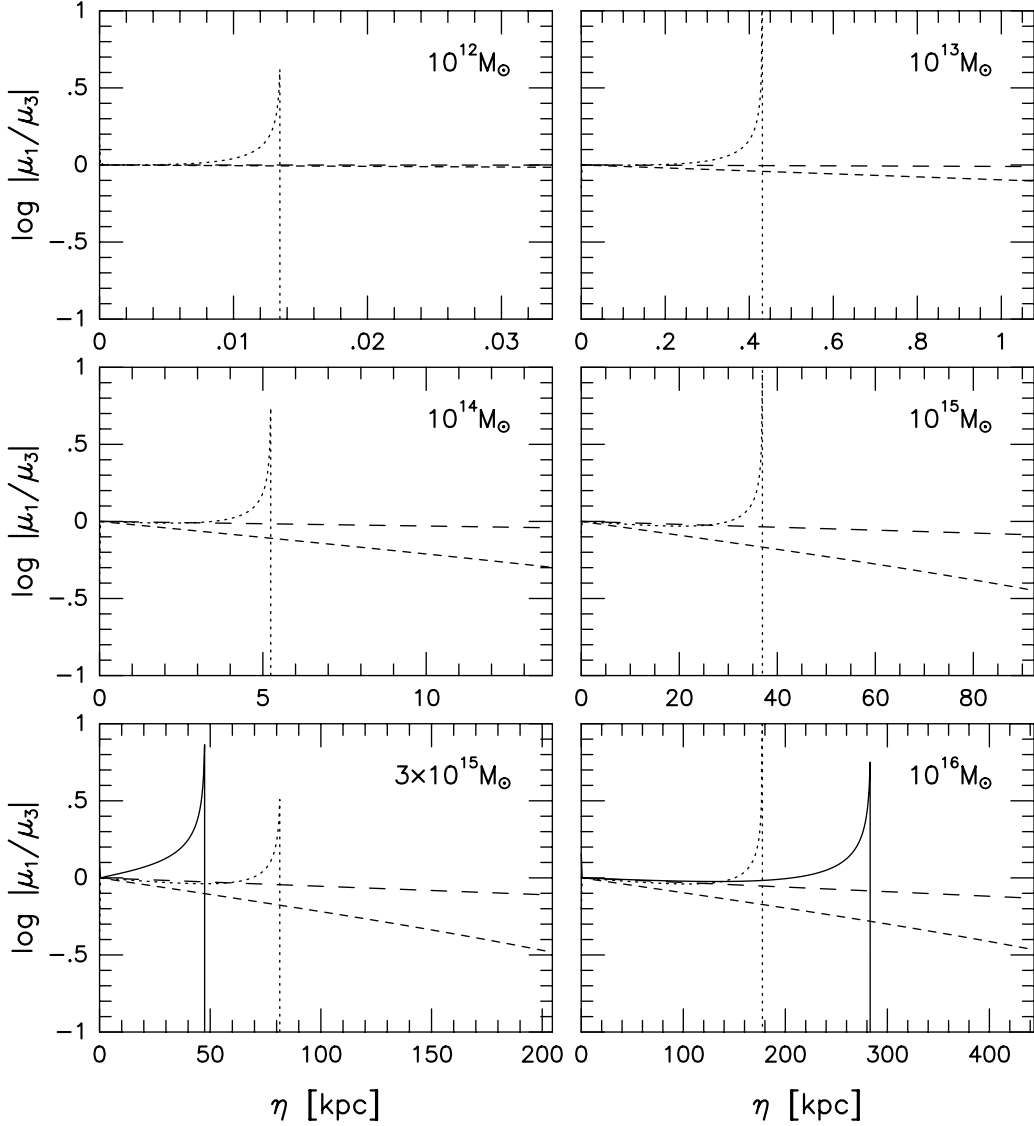


Figure 13. Brightness ratio $|\mu_1/\mu_3|$ versus source location η for lenses of masses $10^{12} - 10^{16} M_\odot$ located at $z_L = 0.5$, for the TIS (solid curves), the NFW profile (dotted curves), the SIS (short dashed curves) and the Schwarzschild lens (long dashed curves).

critical curve, in which case μ_1 diverges. For the ranges of η being considered, The ratio $|\mu_1/\mu_3|$ is always very close to unity for the Schwarzschild lens, and fairly close to unity for the SIS. The TIS and NFW profile do not produce an image 1 at large η , where the source is outside of the radial caustic. Notice that in these figures no curves are plotted for the TIS at small mass, because only one image forms.

The ratio $|\mu_2/\mu_3|$, plotted in Figure 15 for a few cases, is much less interesting. Central image 2, which can be produced only with the TIS or NFW profile, is usually very faint unless it is located near the radial critical curve, in which case it might be too close to image 1 to be resolved individually.

5.3 Shear

The total shear $\gamma(x)$ of an image located at position x is given by

$$\gamma = \left| \frac{m(x)}{x^2} - \kappa(x) \right|, \quad (52)$$

(SEF, eq. [8.15]). For the TIS, we substitute equations (16) and (43) into equation (52), and get

$$\gamma_{\text{TIS}}(x) = \frac{ab\kappa_c}{Ab - Ba} \left| \frac{2A}{x^2} \left[\sqrt{a^2 + x^2} - a \right] - \frac{2B}{x^2} \left[\sqrt{b^2 + x^2} - b \right] - \frac{A}{\sqrt{a^2 + x^2}} + \frac{B}{\sqrt{b^2 + x^2}} \right|. \quad (53)$$

[this result was also obtained by Natarajan, & Lynden-Bell (1997)]. For the NFW profile, the shear is given by

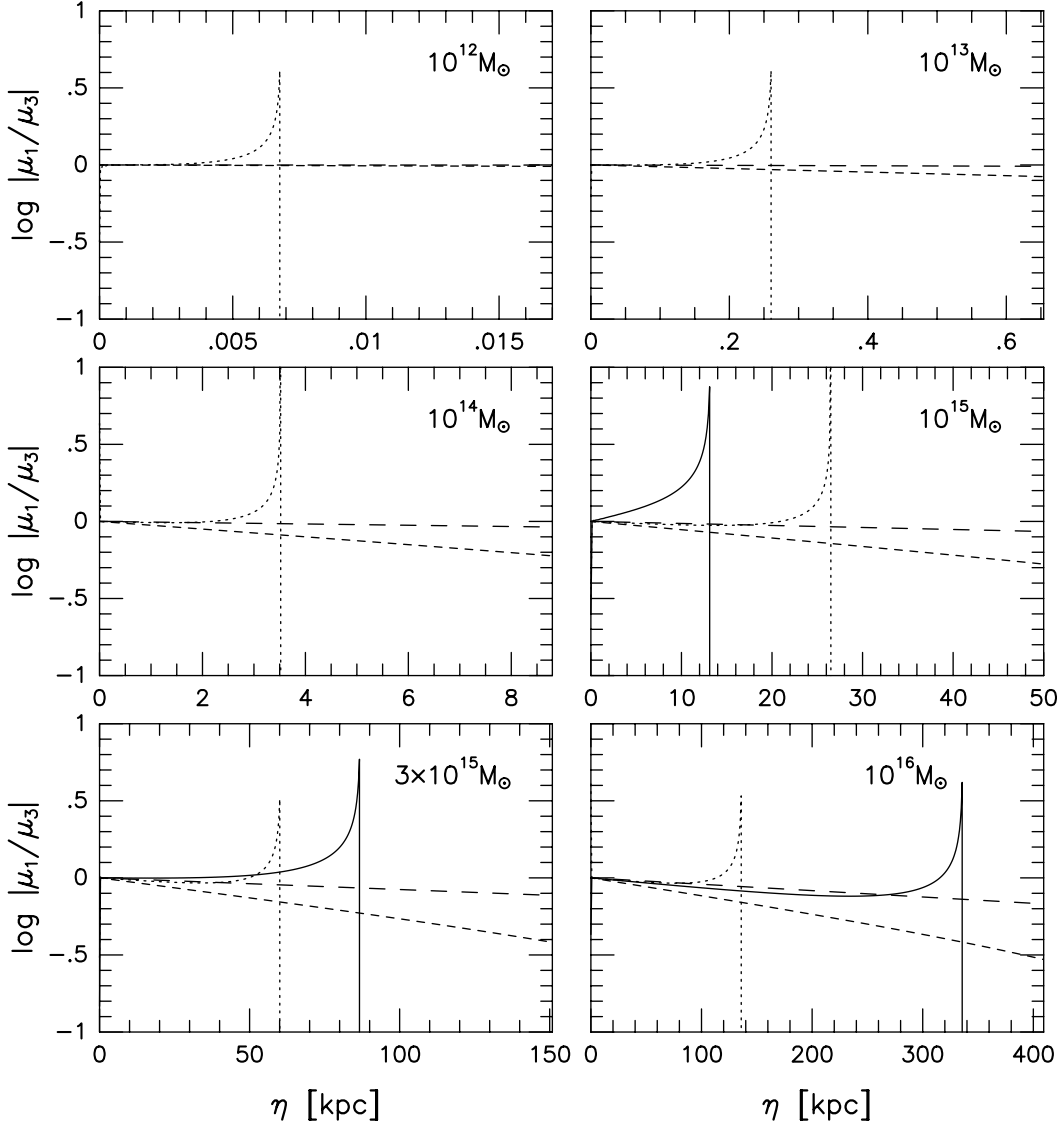


Figure 14. Brightness ratio $|\mu_1/\mu_3|$ versus source location η for lenses of masses $10^{12} - 10^{16} M_\odot$ located at $z_L = 1.0$, for the TIS (solid curves), the NFW profile (dotted curves), the SIS (short dashed curves) and the Schwarzschild lens (long dashed curves).

$$\gamma_{\text{NFW}}(x) = \kappa_s \times \begin{cases} g(x), & x \neq 1; \\ \frac{10}{3} - 4 \ln 2, & x = 1 \end{cases} \quad (54)$$

(Wright & Brainerd 2000). For the SIS, the shear is given by

$$\gamma_{\text{SIS}}(x) = \frac{1}{2|x|} \quad (55)$$

(SEF, page 244). For the Schwarzschild lens, the shear is undefined at $x = 0$ because of the singularity in κ (eq. [19]). Otherwise,

$$\gamma_{\text{Sch}}(x) = \frac{1}{x^2} \quad (56)$$

Figures 16 and 17 show γ_1 and γ_3 (the shear of images 1 and 3) versus source position η for halos located at redshift $z_L = 0.5$ and 1 with various values of M_{200} , and

sources located at redshift $z_S = 3$ (notice that γ_2 is much less interesting, since image 2 is usually very faint). When a pair of curves appear (two curves with the same line type in the same panel), the upper curve corresponds to γ_1 and the lower one to γ_3 , as the shear is always larger for the image located closest to the lens. When only one curve appears, it corresponds to γ_3 .

The Schwarzschild lens always has the largest shear, followed by the SIS. The shear for the TIS is negligible at low masses, but becomes more important as the mass increases, and at $M_{200} = 10^{16} M_\odot$ it exceeds the shear for the NFW profile and is comparable to the shear for the SIS.

In the limit $\eta \rightarrow 0$, the shear converges to the value $\gamma_1, \gamma_3 = 1$ for the Schwarzschild lens and 0.5 for the SIS. The values for the NFW profile and the TIS vary with mass. In the case of the TIS, the shear actually drops to 0 for low masses, when only one image forms (see case $M_{200} =$

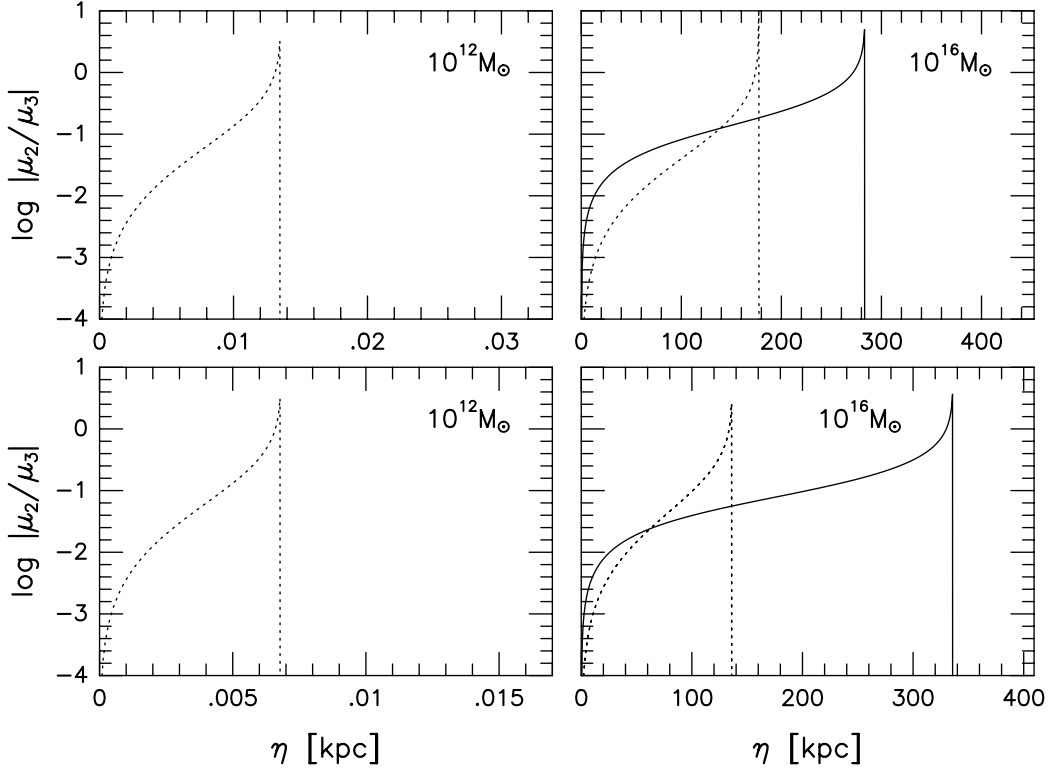


Figure 15. Brightness ratio $|\mu_2/\mu_3|$ versus source location η for lenses of masses 10^{12} and $10^{16} M_\odot$ located at $z_L = 0.5$ and 1 , for the TIS (solid curves) and the NFW profile (dotted curves).

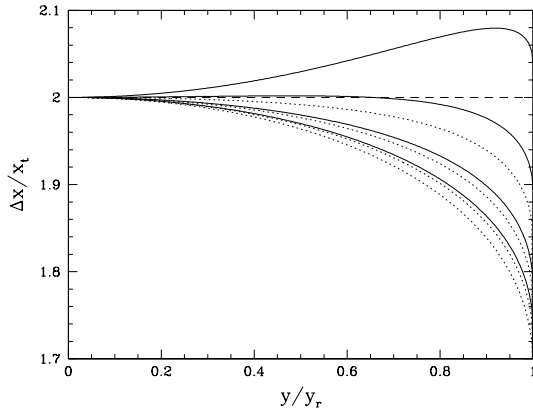


Figure 10. Separation Δx between the two outer images, in units of the tangential critical radius x_t , versus source location y in units of the caustic radius y_r . The solid curves, from top to bottom, corresponds to TIS with $\kappa_c = 10, 5, 2.5,$ and $1.2,$ respectively. The dotted curves, from top to bottom, corresponds to NFW profiles with $\kappa_s = 1.0, 1.0, 0.5,$ and $0.2,$ respectively. The dashed line corresponds to the SIS. Results for the Schwarzschild lens are not plotted.

$10^{15} M_\odot$, $z_L = 1.0$ in Fig. 16). In this case, a circular source near $\eta = 0$ produces a nearly-circular image near $\xi = 0$. For larger masses, the same source produces three images, with two of them (images 1 and 3) located near the tangential critical circle, away from the center, where the shear is large.

The Schwarzschild lens, SIS, and NFW profiles always reach this limit at small enough η , for any value of M_{200} .

5.4 Time Delay

For axially symmetric lenses, the deflection potential $\psi(x)$ is defined by

$$\alpha = \frac{d\psi}{dx}. \quad (57)$$

For a source at location y producing an image at location x , the Fermat potential is defined by

$$\phi(x, y) = \frac{1}{2}(x - y)^2 - \psi(x), \quad (58)$$

and the time delay Δt_{ij} between two images located at x_i and x_j , of a source located at y , is given by

$$\Delta t_{ij}(y) = \frac{\xi_0^2 D_S}{c D_L D_{LS}} (1 + z_L) [\phi(x_i, y) - \phi(x_j, y)] \quad (59)$$

(SEF, eq. [5.44]). Hence, it is trivial to compute the time delay once the deflection potential is known. For the TIS, we integrate equation (36), and get

$$\psi_{\text{TIS}}(x) = \frac{2ab\kappa_c}{Ab - Ba} \left\{ A\sqrt{a^2 + x^2} - B\sqrt{b^2 + x^2} - Aa \ln \left[a + \sqrt{a^2 + x^2} \right] + Bb \ln \left[b + \sqrt{b^2 + x^2} \right] \right\}. \quad (60)$$

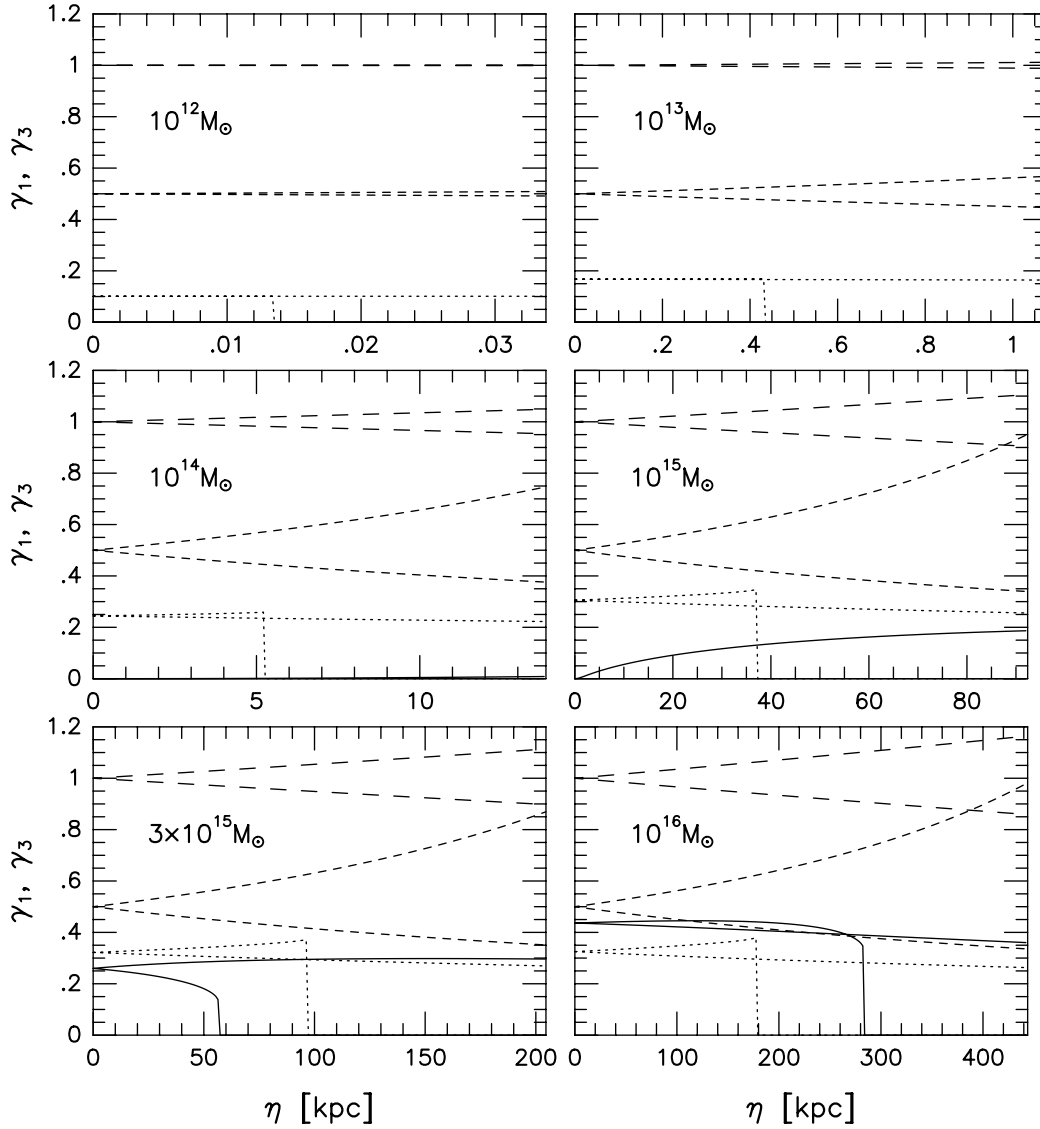


Figure 16. Shear γ_1 and γ_3 of images 1 and 3, versus source location η for lenses of masses $10^{12} - 10^{16} M_\odot$ located at $z_L = 0.5$, for the TIS (solid curves), the NFW profile (dotted curves), the SIS (short dashed curves) and the Schwarzschild lens (long dashed curves). When two curves of the same type appear, the top one is γ_1 , the bottom one γ_3 .

For the NFW profile, we integrate equation (37), and get

$$\psi_{\text{NFW}}(x) = 4\kappa_s \times \begin{cases} \frac{1}{2} \ln^2 \frac{|x|}{2} - 2 \arg \tanh^2 \sqrt{\frac{1-|x|}{1+|x|}}, & |x| < 1; \\ \frac{1}{2} \ln^2 \frac{|x|}{2} + 2 \arctan^2 \sqrt{\frac{|x|-1}{|x|+1}}, & |x| > 1; \end{cases} \quad (61)$$

(Meneghetti, Bartelmann, & Moscardini 2003a,b). For the SIS, the deflection potential is given by

$$\psi_{\text{SIS}}(x) = |x|, \quad (62)$$

and for the Schwarzschild lens,

$$\psi_{\text{Sch}}(x) = \ln |x|. \quad (63)$$

Notice that for general lenses one normally computes the deflection potential ψ first, and then differentiates it to get the deflection angle α , not the other way around. It is the simplicity of spherically symmetric lenses that enables us to compute α directly using equation (31).

The time delay between images 1 and 3 (the two outermost images) is plotted in Figures 18 and 19, for the same range of masses and source location, lens redshift and source redshift as in Figure 11–17. Unlike the magnification and shear, the time delay is not dimensionless, and its value varies tremendously over the ranges of M_{200} and η considered, going from hours to millenia. For the SIS, the

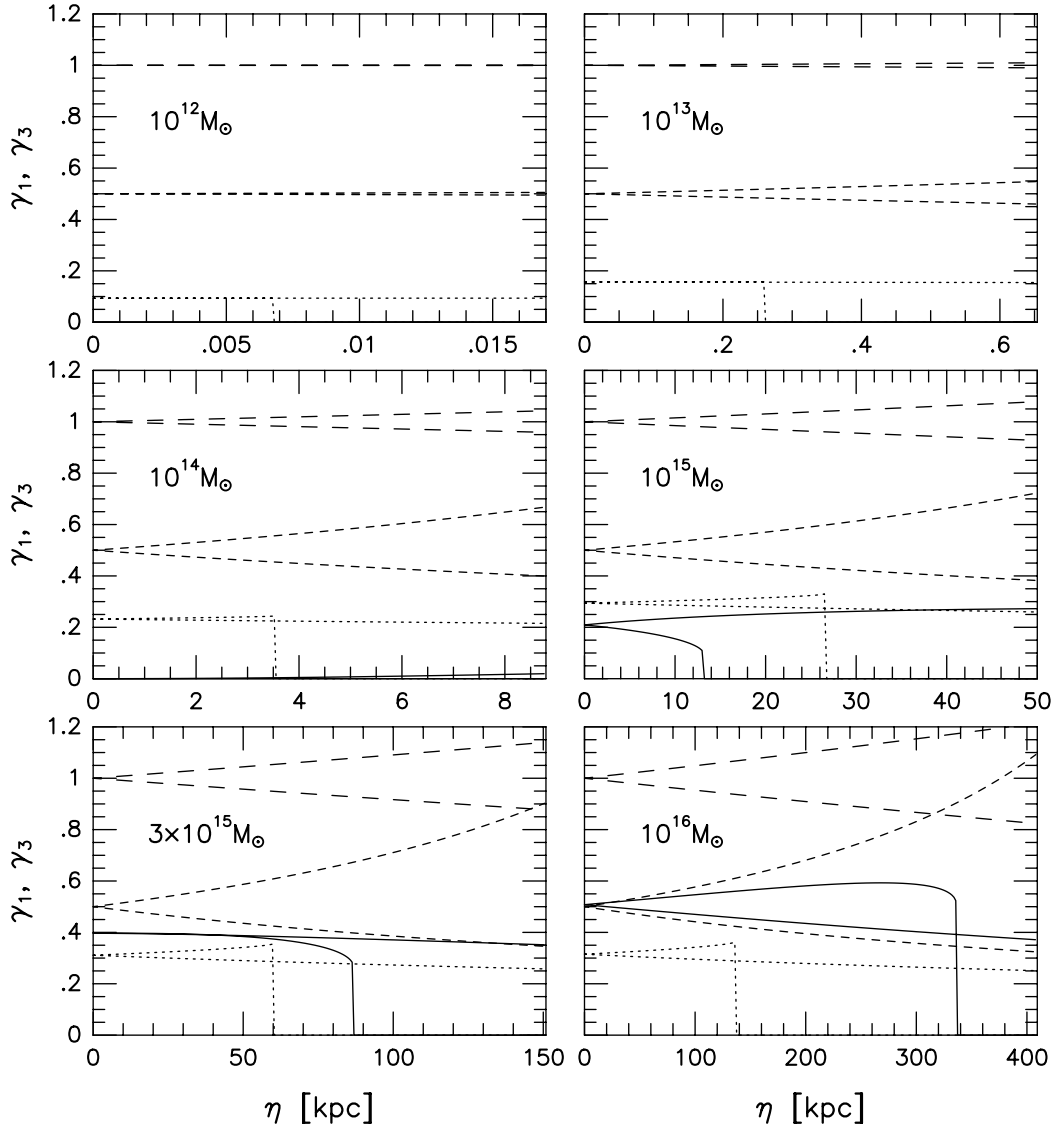


Figure 17. Shear γ_1 and γ_3 of images 1 and 3, versus source location η for lenses of masses $10^{12} - 10^{16} M_\odot$ located at $z_L = 1.0$, for the TIS (solid curves), the NFW profile (dotted curves), the SIS (short dashed curves) and the Schwarzschild lens (long dashed curves). When two curves of the same type appear, the top one is γ_1 , the bottom one γ_3 .

time delay varies linearly with η (SEF, eq. [8.36]). For the Schwarzschild lens, the relation is more complicated (SEF, eq. [8.30]), but reduces to linear at small η .

For the ranges of M_{200} and η considered, the Schwarzschild lens always produces the largest time delay, while the other three profiles produce similar delays with the NFW profile always producing the smallest delay. At low masses, the TIS produces one image, and therefore no time delay, but large masses it produces a larger time delay than either the NFW profile or the SIS. This indicates that there is no simple correspondence between the time delay and the central slope of the density profile.

6 WEAK LENSING

Weak lensing usually refers to the magnification and distortion of the image of a background source by a foreground lens. Unlike strong lensing, weak lensing normally does not produce multiple images of single sources. The detection of coherent distortion patterns in the sky has been used to constrain the mass of clusters. The first detections were reported by Tyson, Wenk, & Valdes (1990); Bonnet, Mellier, & Fort (1994); Dahle, Maddox, & Lilje (1994); Fahlman et al. (1994), and Smail et al. (1995), followed by many others (see Bartelmann & Schneider 2001, and references therein). More recently, the distortion pattern produced by individual galaxies has also been detected

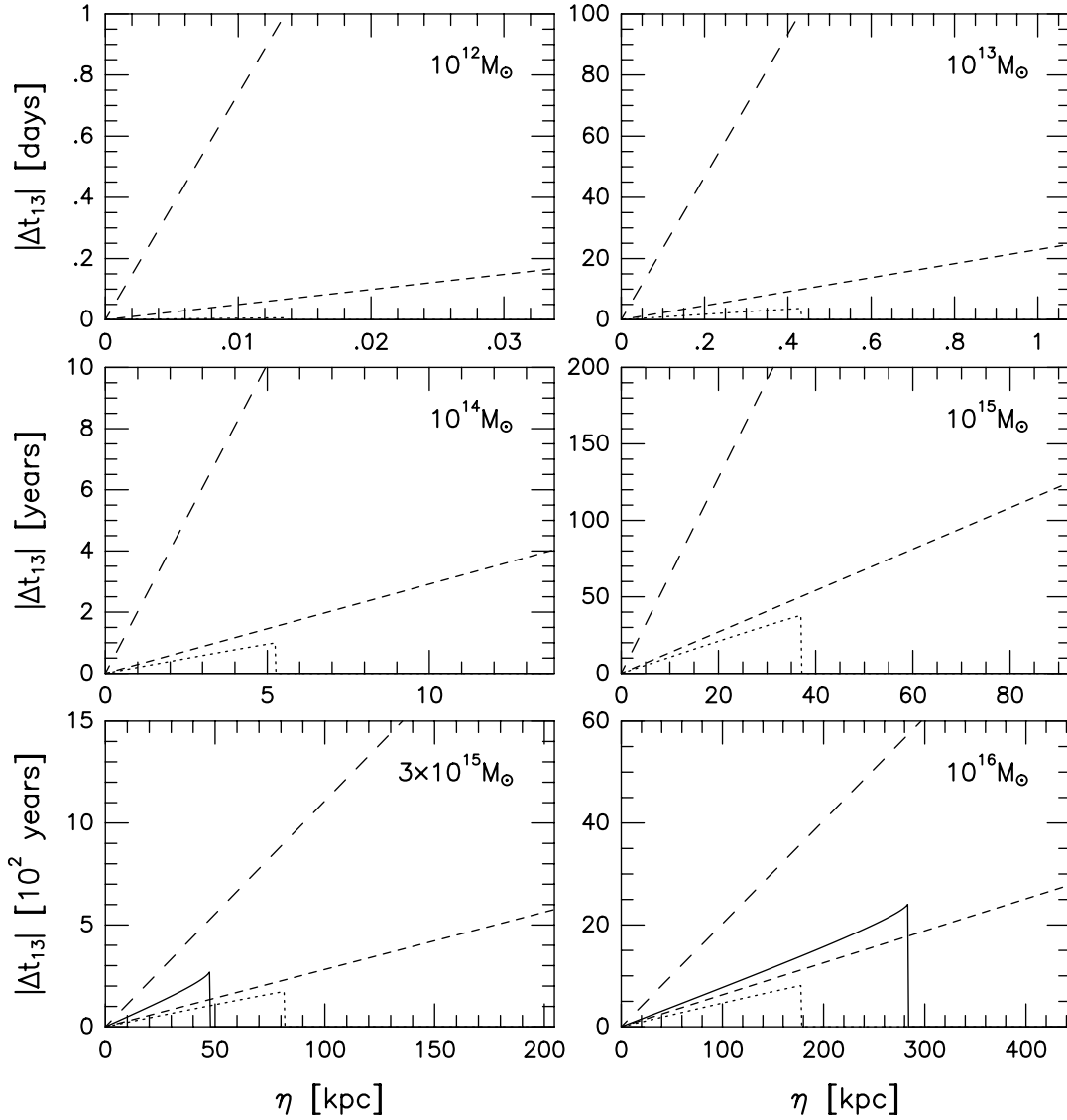


Figure 18. Time delay $|\tau_{13}|$ between images 1 and 3 versus source location η for lenses of masses $10^{12} - 10^{16} M_{\odot}$ located at $z_L = 0.5$, for the TIS (solid curves), the NFW profile (dotted curves), the SIS (short dashed curves) and the Schwarzschild lens (long dashed curves).

(Brainerd, Blandford, & Smail 1996; Griffiths et al. 1996; Dell’Antonio & Tyson 1996; Ebbels 1988; Hudson et al. 1998; Natarajan et al. 1998; Fischer et al. 2000).

Following the approach of Wright & Brainerd (2000), we use as measure of the distortion produced by a lens the average shear $\bar{\gamma}$ inside a distance $\xi = r_{200}$ from the lens center. In practice, this quantity would be evaluated by averaging the shear of all images observed inside r_{200} , after having eliminated foreground sources. We estimate this quantity by integrating the shear over the projected area of the cluster. The average shear inside radius x is given by

$$\bar{\gamma}(x) = \frac{2}{x^2} \int_0^x x' \gamma(x') dx'$$

$$= \frac{2}{x^2} \int_0^x x' \left[\frac{m(x')}{x'^2} - \kappa(x') \right] dx'. \quad (64)$$

We eliminate $m(x')$ using equation (43). The two terms in the integral can easily be computed using equations (57) and (31), respectively. Equation (64) reduces to

$$\bar{\gamma}(x) = \frac{2}{x^2} [\psi(x) - \psi(0)] - \frac{\alpha(x)}{x}. \quad (65)$$

For the Schwarzschild lens, $\psi(x) = \ln|x|$, and therefore $\bar{\gamma}$ diverges because of the term $\psi(0)$ in equation (65). For the SIS, $\alpha(x) = x/|x|$, $\psi(x) = |x|$, and equation (65) reduces to

$$\bar{\gamma}_{\text{SIS}}(x) = \frac{1}{x}. \quad (66)$$

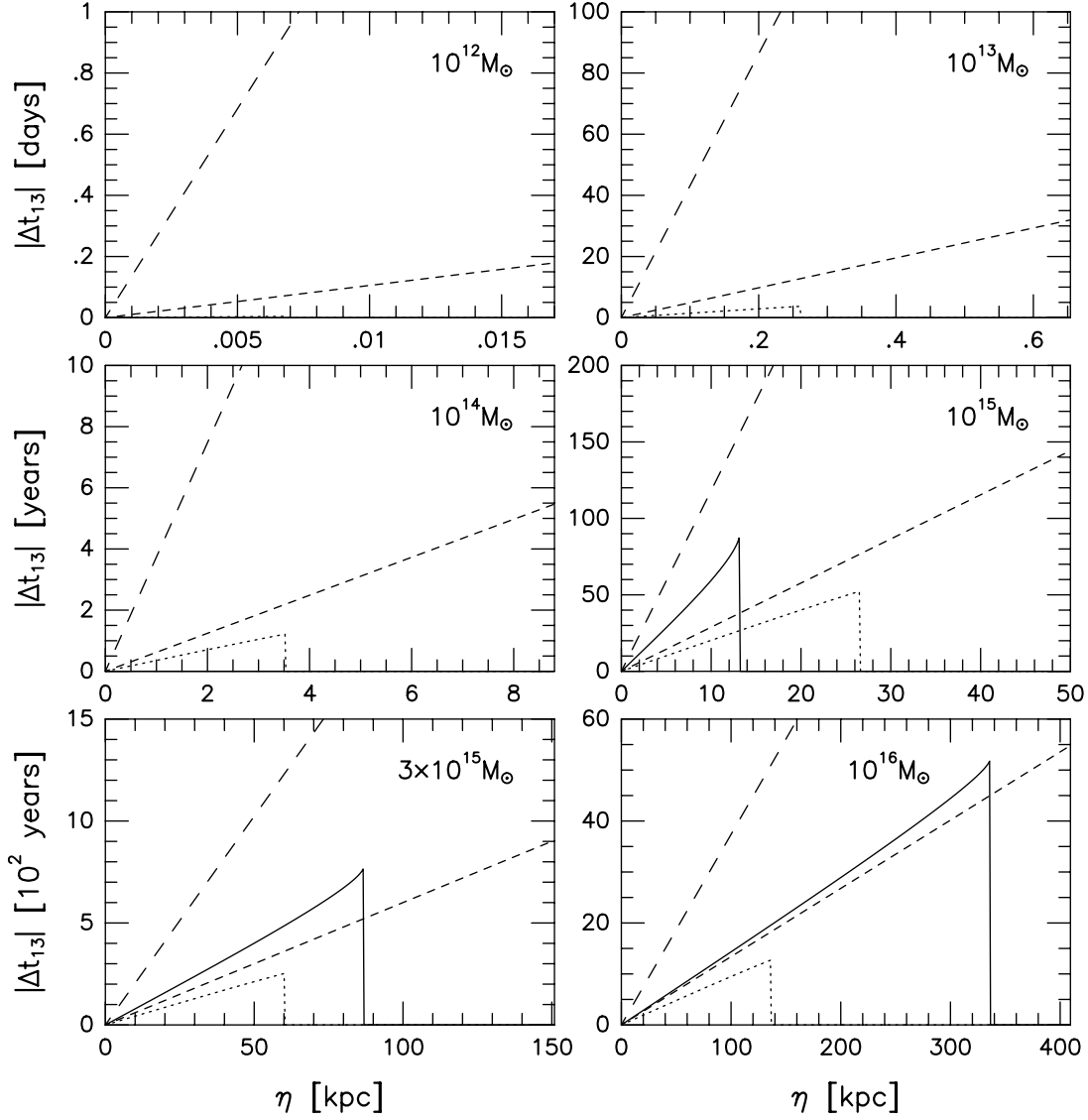


Figure 19. Time delay $|\tau_{13}|$ between images 1 and 3 versus source location η for lenses of masses $10^{12} - 10^{16} M_{\odot}$ located at $z_L = 1.0$, for the TIS (solid curves), the NFW profile (dotted curves), the SIS (short dashed curves) and the Schwarzschild lens (long dashed curves).

We evaluate this expression at $r = r_{200}$, and get

$$\bar{\gamma}_{\text{SIS}}(r_{200}) = \frac{400\pi\rho_c r_{200}}{3\Sigma_{\text{crit}}}, \quad (67)$$

where we used equation (28) to eliminate x_{200} , then equation (39) to eliminate ξ_0 , and finally equation (14) to eliminate σ_V . For the TIS, we substitute equations (36) and (60) in equation (65), and get

$$\bar{\gamma}_{\text{TIS}}(x) = \frac{2ab\kappa_c}{(Ab - Ba)x^2} \times \left\{ Aa \left[\sqrt{1 + \frac{x^2}{a^2}} - 1 - 2 \ln \frac{1 + \sqrt{1 + x^2/a^2}}{2} \right] \right.$$

$$\left. - Bb \left[\sqrt{1 + \frac{x^2}{b^2}} - 1 - 2 \ln \frac{1 + \sqrt{1 + x^2/b^2}}{2} \right] \right\}. \quad (68)$$

We evaluate this expression at $r = r_{200}$, or equivalently $x = r_{200}/r_0 \equiv \eta_{200} = 24.2$. It reduces to

$$\bar{\gamma}_{\text{TIS}}(r_{200}) = 408.67 \frac{\rho_c r_{200}}{\Sigma_{\text{crit}}}, \quad (69)$$

where we used equation (10) to eliminate ρ_0 . Both $\bar{\gamma}_{\text{SIS}}$ and $\bar{\gamma}_{\text{TIS}}$ scale like r_{200} , or $M_{200}^{1/3}$. Their ratio is given by

$$\left(\frac{\bar{\gamma}_{\text{SIS}}}{\bar{\gamma}_{\text{TIS}}} \right) (r = r_{200}) = 1.025, \quad (70)$$

independent of the redshift z_L and mass M_{200} of the lens.

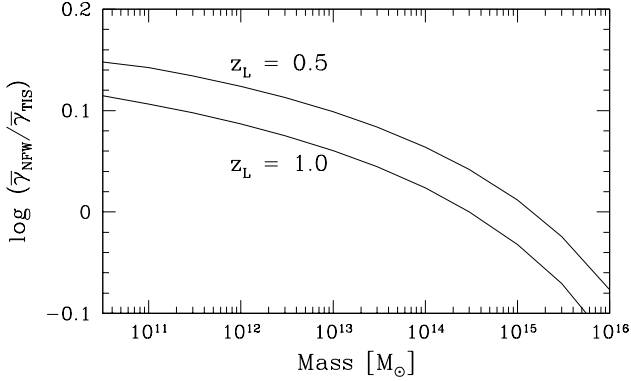


Figure 20. Ratio of the average shear inside radius r_{200} for the NFW profile and the TIS profile, versus mass of the halo, for halos located at redshifts $z_L = 0.5$ and 1 , as indicated.

Furthermore, this result is also independent of our assumptions that the background model is Λ CDM, or the source is located at redshift $z_S = 3$. These enter only in the calculation of Σ_{crit} and ρ_c , which cancel out when we take the ratio of equations (67) and (69). For the NFW profile, we substitute equations (37) and (61) in equation (65), and get

$$\bar{\gamma}_{\text{NFW}} = \frac{4\kappa_s}{x^2} \left[\ln^2 \frac{x}{2} - \ln \frac{x}{2} - 4 \arg \tanh^2 \sqrt{\frac{1-x}{1+x}} - \frac{2}{\sqrt{1-x^2}} \arg \tanh \sqrt{\frac{1-x}{1+x}} \right]. \quad (71)$$

To evaluate this expression at r_{200} , we simply set $x = r_{200}/r_{\text{NFW}} = 1/c$.

In Figure 20, we plot the ratio $\bar{\gamma}_{\text{NFW}}/\bar{\gamma}_{\text{TIS}}$ versus mass, for lenses located at redshifts $z_L = 0.5$ and 1 , and sources located at redshift $z_S = 3$. The ratio $\bar{\gamma}_{\text{NFW}}/\bar{\gamma}_{\text{SIS}}$ can be obtained by shifting the curves down by an amount $\log 1.025 = 0.0107$. The ratios are larger at lower redshifts z_L . They also decrease with increasing mass. This reflects the fact that as the mass increases, the concentration parameter c of the NFW profile decreases, while the ratio r_{200}/r_0 for the TIS remains fixed at 24.2 . This figure can be *qualitatively* compared with the top left panel of Figure 3 in Wright & Brainerd (2000), after the appropriate shifting. Notice, however, that (1) the Λ CDM used by these authors is not exactly the same as the one we use, and (2) these authors used the approach of Navarro, Frenk, & White (1997) to compute the concentration parameter, while we use the more recent approach of Eke et al. (2001). At large enough masses, the average shear produced by the TIS exceeds the one produced by the NFW profile.

We reach essentially the same conclusion as Wright & Brainerd (2000), namely that using the average shear to estimate the mass of lensing halos can lead to considerable errors if the wrong density profile is assumed. At small masses, $\bar{\gamma}_{\text{NFW}}/\bar{\gamma}_{\text{TIS}} > 1$, and therefore the mass of a TIS would be underestimated if the lens is incorrectly assumed to follow a NFW profile. At high mass, the true mass of a TIS would be overestimated.

7 DISCUSSION

In the previous two sections, we derived the effects of strong and weak lensing, respectively. Here, “strong lensing” refers to case with multiple images, arcs, or rings, while “weak lensing” refers to the magnification and shear of single images. We can divide the observed cases of strong lensing in two groups. The first group contains the “arc second” cases: multiple-image systems with image separations of order arc seconds, or rings with radii of that order (see Kochanek et al. 1998).² In most cases, the lens is a single, massive galaxy, with possibly some additional contribution from the environment in which this galaxy is located (Turner, Ostriker, & Gott 1984; see, however, Premadi & Martel 2003). A classic example is Q0957+561, the first gravitational lens to be discovered. The second group contains the “arc minute” cases, in which the lens is an entire cluster of galaxies. These lenses produce mostly giant arcs, with radii in the range $15'' - 60''$ (see Table 1 of Williams, Navarro, & Bartelmann 1999). The most famous case is the cluster CL 0024+1654, which produces multiple arcs.

We showed that for all profiles considered, the image separation is weakly dependent on the source location (Fig. 10), when multiple images actually form. If we neglect this dependence, the image separation $\Delta\theta \approx 2\theta_t$ can be read off the top panels of Figure 6. We see immediately that galaxy-size objects cannot produce arc-second separations if they are described by the TIS or the NFW profile (under the assumptions described in §2 that $z_{\text{coll}} = z_L$ for TIS halos while c for NFW halos is the typical value for halos at $z_{\text{obs}} = z_L$). The TIS does not produce multiple images unless the mass is of order of a cluster mass or above. The NFW profile can produce multiple images for any mass, but a separation $\Delta\theta > 1''$ requires a mass of order $10^{13} M_\odot$. Even the SIS needs a mass in excess of $10^{12} M_\odot$ to produce arc-second separations. At the cluster scale, all profiles are capable of producing arc-minute separations. In this limit, for a given mass, the separation is larger for the Schwarzschild lens, smaller for the NFW profile (because of the small concentration parameter at large mass), and comparable for the SIS and TIS. As we indicated in the introduction, the TIS and NFW profile are applicable to dwarf galaxies and clusters of galaxies, but might not be applicable to ordinary galaxy-scale objects because baryonic processes are neglected. Hence, the inability of the TIS and NFW profiles to produce arc seconds separations with galaxy-size lenses is not a concern.

There is very important caveat to this conclusion. So far, we have assumed that the redshift z_L where the lensing halo is located is the same as the redshift z_{coll} at which this halo first collapsed and virialized. As we pointed out in §2, this does not have to be the case, however, since in principle the halo could have collapsed at any redshift $z_{\text{coll}} \geq z_L$. Consider for instance the TIS. The central density ρ_0 is determined by equation (10), and so far we have assumed that $\rho_c(z)$ was evaluated at z_L . But if $z_{\text{coll}} > z_L$, then $\rho_c(z)$ must be evaluated at z_{coll} , instead. By combining equations (6), (7), (10), and (35), and get

² See <http://cfa-www.harvard.edu/castles>.

$$\kappa_c \propto \frac{\rho_0 r_0}{\Sigma_{\text{crit}}(z_L)} \propto \frac{M_{200}^{1/3} \rho_c^{2/3}(z_{\text{coll}})}{\Sigma_{\text{crit}}(z_L)}. \quad (72)$$

Hence, for a given mass, increasing z_{coll} will result in an increase in κ_c , and lensing will be stronger. Similarly, a particular effect (for instance, production of multiple images, which requires $\kappa_c > 1$) can be achieved with a smaller mass halo if that halo collapsed earlier. For the NFW profile, the expressions for the characteristic radius and density, equations (11) and (12), depend on the concentration parameter c . The models that describe the dependence of c on M_{200} , and z (Navarro, Frenk, & White 1997; Eke, Navarro, & Steinmetz 2001) already take into account the difference between z and z_{coll} . Hence, unlike the case for the TIS, we are not free to set the redshift z to any other value than z_L in equation (12). However, as we explained in §2, the value of c we have used so far, which is a single function of M_{200} and z_L , is a statistical average over many realizations, and a particular halo might have a different concentration parameter.

Let us now focus on the TIS, and perform a simple calculation to estimate the probability that a TIS can produce multiple images. To compute κ_c , we substitute equations (6), (7), and (10) in equation (35). For the particular cosmological model (Λ CDM) and redshifts ($z_S = 3$, $z_L = 0.5, 1.0$) we have considered in this paper, we get

$$\begin{aligned} \kappa_c &= 480.75 \frac{\rho_c^{2/3}(z_L)}{\Sigma_{\text{crit}}(z_L)} \left[\frac{\rho_c(z_{\text{coll}})}{\rho_c(z_L)} \right]^{2/3} M_{200}^{1/3} \\ &= \left[\frac{\rho_c(z_{\text{coll}})}{\rho_c(z_L)} \right]^{2/3} M_{15}^{1/3} \times \begin{cases} 0.968, & z_L = 0.5; \\ 1.289, & z_L = 1.0; \end{cases} \end{aligned} \quad (73)$$

where $M_{15} \equiv M_{200}/10^{15} M_\odot$. Strong lensing requires $\kappa_c > 1$. If $z_L = z_{\text{coll}}$, this condition becomes

$$M_{15} \geq \begin{cases} 1.102, & z_L = 0.5; \\ 0.467, & z_L = 1.0 \end{cases} \quad (74)$$

(these values are the location of the cutoffs in Fig. 6). For the cosmological model we consider, a $1\text{-}\sigma$ density fluctuation collapsing at redshift $z_{\text{coll}} = 0.5$ (1.0) has a mass of about $M_{15} = 2 \times 10^{-3}$ (4×10^{-4}). Such ‘‘typical’’ objects will not be capable of producing multiple images of a source at redshift $z_S = 3$, since the resulting value $\kappa_c = 0.122$ (0.095) is smaller than unity. This simply indicates that multiple images are not produced by the typical objects that collapse at $z_{\text{coll}} = z_L$, which is certainly consistent with the fact that fewer than 100 multiple-image systems have been observed.

Increasing κ_c above unity would require an object about a thousand times more massive than a typical object at the same redshift. Objects of this mass are rare but do exist. We can make a simple estimate of how atypical such a massive object is. Over most of the mass range of cosmological interest (from small galaxies to clusters of galaxies) the CDM power spectrum can be roughly approximated by a power law $P(k) \propto k^n$, where k is the wavenumber and $n \approx -2$. The rms density fluctuation δ_{rms} is then given by $\delta_{\text{rms}} \approx k^{3/2} P^{1/2}(k) \propto k^{1/2}$. At a given redshift, different values of the wavenumber k correspond to different mass scales M according to $M \propto k^{-3}$. The relation between rms density fluctuation and mass scale at fixed epoch is therefore approximated by

$$\delta_{\text{rms}} \propto M^{-1/6}. \quad (75)$$

Increasing the mass by a factor of 1000 therefore reduces δ_{rms} by a factor of $1000^{1/6} \approx 3$. Because of the reduction in δ_{rms} , a $1\text{-}\sigma$ fluctuation ($\delta = \delta_{\text{rms}}$) at this higher mass will no longer collapse by the same redshift (it will collapse later), but a $3\text{-}\sigma$ fluctuation ($\delta = 3\delta_{\text{rms}}$) will. Such fluctuations are rare, but not vanishingly rare. In Gaussian statistics, the probability that a randomly located point in space is inside a $3\text{-}\sigma$ density fluctuation (i.e. $\delta \geq 3\delta_{\text{rms}}$) is $1/384$. Hence, one of every 384 halos would be capable of producing multiple images (of course, whether any halo actually produces multiple images depends on the location of the sources). This was derived by assuming $z_{\text{coll}} = z_L$. As equation (73) shows, the condition $\kappa_c > 1$ can be satisfied with a smaller mass if we assume that the halo collapsed at an earlier redshift $z_{\text{coll}} > z_L$.

A similar calculation could be carried out for the NFW profile. In this case, at fixed mass M_{200} and redshift z_L , we are free to choose a concentration parameter c that differs from the statistical average corresponding to this mass and redshift. If we then combine equations (11), (12), and (38), and ignore the weak dependence of the denominator of equation (12) on c at large c , we get

$$\kappa_s = \frac{\rho_{\text{NFW}} r_{\text{NFW}}}{\Sigma_{\text{crit}}(z_L)} \propto \frac{c^2 M_{200}^{1/3} \rho_c^{2/3}(z_L)}{\Sigma_{\text{crit}}(z_L)}. \quad (76)$$

Hence, we can increase the effect of lensing, or reduce the minimum mass necessary to produce a particular effect, by increasing the concentration parameter.

The simple calculations presented in this discussion were for illustration purpose only. In a future paper, we will present a detailed calculation of the expected frequency of multiple image systems for comparison with the statistics of observed lensing.

8 SUMMARY AND CONCLUSION

We have derived the lensing properties of cosmological halos described by the Truncated Isothermal Sphere model. The solutions depend on the background cosmological model through the critical surface density Σ_{crit} , which is a function of the cosmological parameters and the source and lens redshifts, and the TIS parameters ρ_0 and r_0 , which are functions of the mass and collapse redshift of the halo, and the cosmological parameters. By expressing the surface density of the halo in units of Σ_{crit} and the distances in units of r_0 , all explicit dependences on the cosmological model disappear, and the solutions are entirely expressible in terms of two dimensionless parameters, the central convergence κ_c and the scaled position y of the source. We have computed solutions for the critical curves and caustics, the image separations, the magnification and brightness ratios, the shear, and the time delay. The ability of the TIS to produce strong lensing (multiple images and rings) depends entirely on κ_c . If $\kappa_c < 1$, only one image can form. If $\kappa_c > 1$, either one or three images can form, depending on whether the source is located outside or inside the radial caustic. When three images are produced, the central one is usually very faint, being highly demagnified. Degenerate image configurations occur when an extended source overlaps a caustic. Two images are produced when the source overlaps the radial caustic, while an Einstein ring with a central spot is produced when the source overlaps the tangential caustic, which is a single

point located at $y_t = 0$. These degenerate cases correspond to maxima of the total magnification, which diverges as the source size goes to zero. When three images are produced, the angular separation between the two outermost images depends strongly on κ_c , but only weakly on the source location.

For comparison, we derived (or extracted from the literature) the lensing properties of three comparison models: the NFW profile, the singular isothermal sphere, and the Schwarzschild lens. Unlike the TIS, all of these profiles have a central singularity, which allows them to produce multiple images at any mass, provided that the source is sufficiently aligned with the lens. In practice, image separations large enough to be resolved can be achieved by galactic-mass objects only for the Schwarzschild lens, and by supergalactic-mass objects for all profiles.

This paper focused on the intrinsic properties of individual lenses described by the TIS model and the comparison models. It provides all the necessary formulae one needs to study gravitational lensing by the TIS, and the comparison profiles, in specific cosmological models. We will present such studies in forthcoming papers. As an illustration here, we applied the TIS model to the currently-favored Λ CDM universe, to calculate the central convergence κ_c expected for TIS halos of different masses and collapse epochs. We found that high-redshift sources (e.g. $z_S \approx 3$) will be strongly lensed by TIS halos (i.e. $\kappa_c > 1$) only for cluster-mass halos, assuming that these halos formed at the redshift they are observed. As equation (73) shows, the halo mass required for strong lensing can be decreased by increasing the formation redshift of the halo. An example of a lens for which $z_{\text{coll}} > z_L$ is discussed by Shapiro & Iliev (2000), who showed that the mass-model derived by Tyson, Kochanski & Dell'Antonio (1998) to explain their lensing data for cluster CL 0024+1654 at $z = 0.39$ is very well-fit by a TIS halo with $\rho_0 \approx 0.064h^2 M_\odot \text{pc}^{-3}$ and $r_0 \approx 20h^{-1} \text{kpc}$. This central density implies that the halo collapse redshift is $z_{\text{coll}} \approx 2.5$ (i.e. $z_{\text{coll}} \gg z_L$).

ACKNOWLEDGMENTS

We thank J. Navarro for providing the FORTRAN subroutine `cons.f` for computing the concentration parameter for the NFW profile. This work was supported by NASA ATP Grants NAG5-10825 and NAG5-10826, and Texas Advanced Research Program Grant 3658-0624-1999.

REFERENCES

- Bartelmann, M. 1996, *A&A*, 313, 697
 Bartelmann, M., & Schneider, P. 2001, *Phys.Rep.*, 340, 291
 Binney, J., & Tremaine, S. 1987, *Galactic Dynamics* (Princeton: Princeton University Press)
 Blandford, R. D., Saust, A. B., Brainerd, T. G., & Villumsen, J. V. 1991, *MNRAS*, 251, 600
 Bonnet, H., Mellier, Y., & Fort, B. 1994, *ApJ*, 427, L83
 Brainerd, T. G., Blandford, R. D., & Smail, I. 1996, *ApJ*, 466, 623
 Burkert, A., 1995, *ApJ*, 447, L25
 Burkert, A., & Silk, J. 1999, in *Dark Matter in Astrophysics and Particle Physics*, Proceedings of the second International Conference on Dark Matter in Astrophysics and Particle Physics, eds. H. V. Klapdor-Kleingrothaus and L. Baudis (Philadelphia: Institute of Physics Publishers), p. 375
 Cen, R. 2001, *ApJ*, 546, L77
 Chiba, T., & Takahashi, R. 2001, unpublished (astro-ph/0106273 v1)
 Chiba, T., & Takahashi, R. 2002, *Prog.Theor.Phys.*, 107, L625
 Cole, S., & Lacey, C. 1996, *MNRAS*, 281, 716
 Colín, P., Avila-Reese, V., & Valenzuela, O. 2000, *ApJ*, 542, 622
 Dahle, H., Maddox, S. J., & Lilje, P. B. 1994, *ApJ*, 435, L79
 Davé, R., Spergel, D. N., Steinhardt, P. J., & Wandelt, B. D. 2001, *ApJ*, 547, 574
 Dell'Antonio, I., & Tyson, J. A. 1996, *ApJ*, 473, L17
 Dressler, A., Smail, I., Poggianti, B. M., Butcher, H., Couch, E. J., Ellis, R. S., & Oemler, A. 1999, *ApJS*, 122, 51
 Ebbels, T. 1998, Ph.D. thesis, Cambridge Univ.
 Eke, V. R., Navarro, J. F., & Steinmetz, M. 2001, *ApJ*, 554, 114
 El-Zant, A., Shlosman, I., & Hoffman, Y. 2001, *ApJ*, 560, 636
 Evrard, A. E., et al. 2002, *ApJ*, 573, 7
 Evrard, A. E., Metzler, C. A., & Navarro, J. F. 1996, *ApJ*, 469, 494
 Fahlman, G., Kaiser, N., Squires, G., & Woods, D. 1994, *ApJ*, 437, 56
 Fischer, P. et al. 2000, *AJ*, 120, 1198
 Fukushige, T., & Makino, J. 1997, *ApJ*, 477, L9
 Fukushige, T., & Makino, J. 2001a, *ApJ*, 557, 533
 Fukushige, T., & Makino, J. 2001b, preprint (astro-ph/0108014)
 Gelato, S., & Sommer-Larsen, J. 1999, *MNRAS*, 303, 321
 Ghigna, S., Moore, B., Governato, F., Lake, G., Quinn, T., & Stadel, J. 2000, *ApJ*, 544, 616
 Goodman, J. 2000, *New Astronomy*, 5, 103
 Griffiths, R. E., Casertano, S., Im, M., & Ratnatunga, K. U. 1996, *MNRAS*, 282, 1159
 Hannestad, S., & Scherrer, R. J. 2000, *Phys.Rev.D.*, 62, 043522
 Hinshaw, G., & Krauss, L. M. 1987, *ApJ*, 320, 468
 Hu, W., Barkana, R., & Gruzinov, A. 2000, *Phys.Rev.Lett.*, 85, 1158
 Hudson, M. J., Gwyn, S. D. J., Dahle, H., & Kaiser, N. 1998, *ApJ*, 503, 531
 Huss, A., Jain, B., & Steinmetz, M. 1999, *MNRAS*, 308, 1011
 Iliev, I. T. 2000, PhD Thesis (University of Texas at Austin)
 Iliev, I. T., & Shapiro, P. R. 2001a, *MNRAS*, 325, 468 (Paper II)
 Iliev, I. T., & Shapiro, P. R. 2001b, preprint (astro-ph/0112427)
 Jaroszyński, M. 1991, *MNRAS*, 249, 430
 Jaroszyński, M. 1992, *MNRAS*, 255, 655
 Jing, Y., & Suto, Y. 2000, *ApJ*, 526, L69
 Kaplinghat, M., Knox, L., & Turner, M. S. 2000,

- Phys.Rev.Lett., 85, 3335
- Keeton, C. R., & Madau, P., 2001, ApJ, 549, L29
- Klypin, A., Kravtsov, A. V., Bullock, J. S., & Primack, J. R. 2000, preprint (astro-ph/0006343)
- Kochanek, C. S. 1995, ApJ, 453, 545
- Kochanek, C. S., Falco, E. E., Impey, C., Lahár, J., McLeod, B., & Rix, H.-W. 1998, CASTLE Survey Gravitational Lens Data Base (Cambridge:CfA)
- Li, L.-X., & Ostriker, J. P. 2002, ApJ, 566, 652
- Martel, H., Premadi, P., & Matzner, R. 2002, ApJ, 570, 17
- Meneghetti, M., Bartelmann, M., & Moscardini, L. 2003a, MNRAS, 340, 105
- Meneghetti, M., Bartelmann, M., & Moscardini, L. 2003b, preprint (astro-ph/0302603)
- Moore, B. 2001, in AIP Conf. Series 586, Relativistic Astrophysics, Proceedings of the 20th Texas Symposium, eds. J. C. Wheeler & H. Martel, p. 73
- Moore, B., Governato, F., Quinn, T., Stadel, J., & Lake, G. 1998, ApJ, 499, L5
- Moore, B., Quinn, T., Governato, F., Stadel, J., & Lake, G. 1999, MNRAS, 310, 1147
- Narayan, R., & White, S. D. M. 1988, MNRAS, 231, 97p
- Natarajan, P., Kneib, J.-P., Smail, I., & Ellis, R. S. 1998, ApJ, 499, 600
- Natarajan, P., & Lynden-Bell, D. 1997, MNRAS, 286, 268
- Navarro, J. F., Frenk, C. S., & White, S. D. M. 1996, ApJ, 462, 563
- Navarro, J. F., Frenk, C. S., & White, S. D. M. 1997, ApJ, 490, 493
- Peebles, P. J. E. 2000, ApJ, 534, L127
- Power, C., Navarro, J. F., Jenkins, A., Frenk, C. S., White, S. D. M., Springel, V., Stadel, J., & Quinn, T. 2002, submitted to MNRAS (astro-ph/0201544)
- Premadi, P., & Martel, H. 2003, in preparation
- Premadi, P., Martel, H., & Matzner, R. 1998, ApJ, 493, 10
- Premadi, P., Martel, H., Matzner, R., & Futamase, T. 2001a, ApJ Suppl., 135, 7
- Premadi, P., Martel, H., Matzner, R., & Futamase, T. 2001b, P.A.S.Aus., 18, 201
- Primack, J. R., Bullock, J. S., Klypin, A. A., & Kravtsov, A. V. 1999, in ASP Conf. Ser. 182, Galaxy Dynamics, ed. D. R. Merritt, M. Valluri, and J. A. Sellwood (San Francisco: ASP)
- Rusin, D., & Ma, C.-P. 2001, ApJ, 549, L33
- Schneider, P., Ehlers, J., & Falco, E. E. 1992, Gravitational Lenses (New York: Springer) (SEF)
- Shapiro, P. R., & Iliev, I. T. 2000, ApJ, 542, L1
- Shapiro, P. R., Iliev, I. T., & Raga, A. C. 1999, MNRAS, 307, 203 (Paper I)
- Smail, I., Ellis, R. S., Fitchett, M. J., & Edge, D. 1995, MNRAS, 273, 277
- Sommer-Larsen, J., & Dolgov, A. 2001, ApJ, 551, 608
- Soucail, G. 2001, in AIP Conf. Series 586, Relativistic Astrophysics, Proceedings of the 20th Texas Symposium, eds. J. C. Wheeler & H. Martel, p. 233
- Spergel, D. N., & Steinhardt, P. J. 2000, Phys.Rev.Lett., 84, 3760
- Takahashi, R., & Chiba, T. 2001, ApJ, 563, 489
- Tormen, G., Bouchet, F. R., & White, S. D. M. 1997, MNRAS, 286, 865
- Turner, E. L., Ostriker, J. P., & Gott, J. R. 1984, ApJ, 284, 1
- Tyson, J. A., Kochanski, G. P., & Dell'Antonio, I. P. 1998, ApJ, 498, L107
- Tyson, J. A., Wenk, R. A., & Valdes, F. 1990, ApJ, 349, L1
- van den Bosch, F. C., & Swaters, R. A. 2001, MNRAS, 325, 1017
- Williams, L. L. R., Navarro, J. F., & Bartelmann, M. 1999, ApJ, 527, 535
- Wright, C. O., & Brainerd, T. G. 2000, ApJ, 534, 34
- Wyithe, J. S. B., Turner, E. L., & Spergel, D. N. 2001, ApJ, 555, 504
- Yoshida, N., Springel, V., White, S. D. M., & Tormen, G. 2000, ApJ, 544, L87
- Young, P., Gunn, J. E., Kristian, J., Oke, J. B., & Westphal, J. A. 1980, ApJ, 241, 507

This paper has been typeset from a $\text{\TeX}/\text{\LaTeX}$ file prepared by the author.